

Acyl-CoA synthetase 3 promotes lipid droplet biogenesis in ER microdomains

Adam Kassan,¹ Albert Herms,¹ Andrea Fernández-Vidal,¹ Marta Bosch,¹ Nicole L. Schieber,^{2,3} Babu J.N. Reddy,⁴ Alba Fajardo,¹ Mariona Gelabert-Baldrich,¹ Francesc Tebar,^{1,5} Carlos Enrich,^{1,5} Steven P. Gross,⁴ Robert G. Parton,^{2,3} and Albert Pol^{1,5,6}

¹Equip de Senyalització i Proliferació Cel·lular, Institut d'Investigacions Biomèdiques August Pi i Sunyer (IDIBAPS), 08036 Barcelona, Spain

²The Institute for Molecular Bioscience and ³Centre for Microscopy and Microanalysis, The University of Queensland, Brisbane, Queensland 4072, Australia

⁴Department of Developmental and Cell Biology, University of California, Irvine, Irvine, CA 92697

⁵Departament de Biologia Cel·lular, Immunologia i Neurociències, Facultat de Medicina, Universitat de Barcelona, 08036 Barcelona, Spain

⁶Institució Catalana de Recerca i Estudis Avançats (ICREA), 08010 Barcelona, Spain

Control of lipid droplet (LD) nucleation and copy number are critical, yet poorly understood, processes. We use model peptides that shift from the endoplasmic reticulum (ER) to LDs in response to fatty acids to characterize the initial steps of LD formation occurring in lipid-starved cells. Initially, arriving lipids are rapidly packed in LDs that are resistant to starvation (pre-LDs). Pre-LDs are restricted ER microdomains with a stable core of neutral lipids. Subsequently, a first round of "emerging" LDs is nucleated, providing additional

lipid storage capacity. Finally, in proportion to lipid concentration, new rounds of LDs progressively assemble. Confocal microscopy and electron tomography suggest that emerging LDs are nucleated in a limited number of ER microdomains after a synchronized stepwise process of protein gathering, lipid packaging, and recognition by Plin3 and Plin2. A comparative analysis demonstrates that the acyl-CoA synthetase 3 is recruited early to the assembly sites, where it is required for efficient LD nucleation and lipid storage.

Introduction

Lipid droplets (LDs) are ubiquitous organelles that collect, store, and supply lipids (Walther and Farese, 2012). Nonetheless, excessive or reduced accumulations of LDs are hallmarks of prevalent human diseases including steatohepatitis, obesity, diabetes, myopathies, arteriosclerosis, or lipodystrophies. However, relatively little is known about the molecular processes and sites that control LD formation. In eukaryotes, LDs likely form de novo by accumulation of neutral lipids in the ER. Consistent with this, the ER harbors enzymes required for neutral lipid synthesis (Buhman et al., 2001), many ER proteins are required for LD formation and expansion (Brasaemle and Wolins, 2012), LDs can be generated in vitro with ER microsomes (Lacey et al., 1999; Marchesan et al., 2003), and there exists an active partitioning of proteins between the ER and LDs (Jacquier et al., 2011). However, although it has been possible

to detect early LDs in the proximity of the ER (Pol et al., 2004; Wolins et al., 2005; Turró et al., 2006; Kuerschner et al., 2008; Skinner et al., 2009; Poppelreuther et al., 2012), whether these are indeed nascent LDs, and whether specialized microdomains existed before the recruitment of these proteins was unknown. Indeed, it was commonly assumed that direct imaging of newly forming LDs was impossible with the current methodology (Salo et al., 2011; Suzuki et al., 2011).

The generally accepted model is that triglycerides are deposited as a lens within the ER bilayer. This process is presumably regulated by proteins, as LD formation is not spontaneously triggered by accumulation of neutral lipids in the ER (Gubern et al., 2008; Adeyo et al., 2011). Thus, ER proteins that can extend hydrophobic domains into the bilayer are attractive candidates to recognize and organize the sites of nucleation. We previously identified a localization signal for sorting proteins with a hydrophobic domain within

A. Kassan, A. Herms, and A. Fernández-Vidal contributed equally to this paper. Correspondence to Robert G. Parton: r.parton@imb.uq.edu.au; or Albert Pol: apols@ub.edu

Abbreviations used in this paper: ACSL, acyl-CoA synthetase long-chain family; LD, lipid droplet; OA, oleic acid; OFP, orange fluorescent protein; pre-LD, pre-existing LD; qRT-PCR, quantitative RT-PCR.

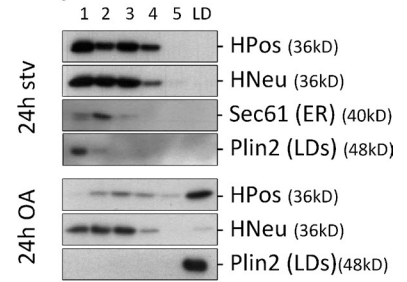
© 2013 Kassan et al. This article is distributed under the terms of an Attribution-Noncommercial-Share Alike-No Mirror Sites license for the first six months after the publication date (see <http://www.rupress.org/terms>). After six months it is available under a Creative Commons License (Attribution-Noncommercial-Share Alike 3.0 Unported license, as described at <http://creativecommons.org/licenses/by-nc-sa/3.0/>).

Supplemental Material can be found at:
[/content/suppl/2013/12/20/jcb.201305142.DC1.html](http://content.suppl/2013/12/20/jcb.201305142.DC1.html)

A Model peptides: HPos and HNeu

	ALDI's hydrophobic domain	Positive Sequence	
HPos:	mdvlpvllqllvllltlplhllallgcwq - p - lfeai gk ifsnir ist gkei	(pI 9.0)	
		Neutral Sequence	
HNeu:	mdvlpvllqllvllltlplhllallgcwq - p - lfeai g ifsn ig istggei	(pI 3.8)	

B Peptides distribution



Intracellular distribution of HPos and HNeu

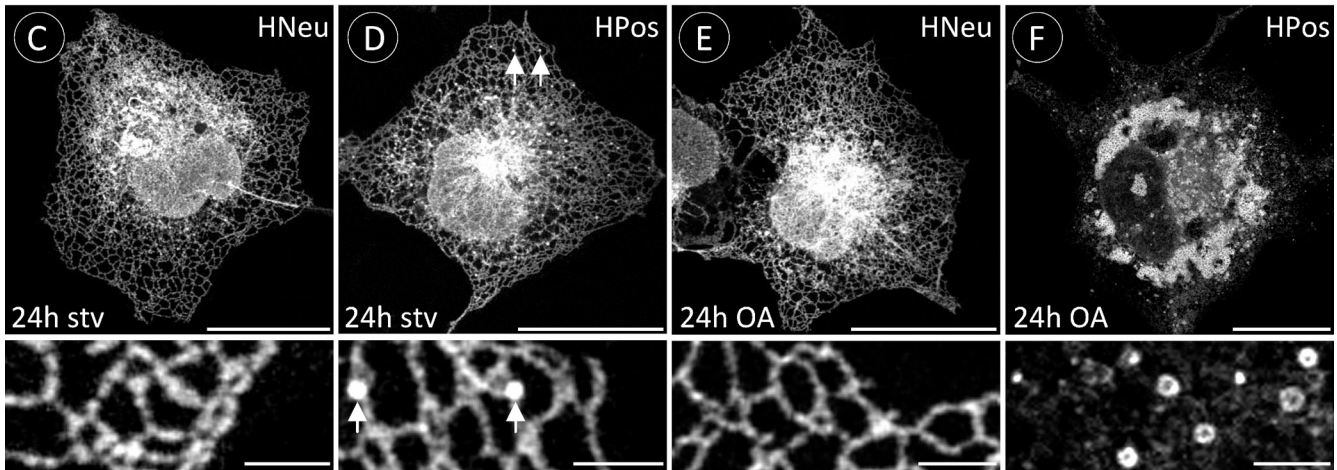


Figure 1. **ER into LD segregation of HPos.** (A) Model peptides used in this work. Bold letters indicate the three positive residues that were mutated to glycines. (B) Starved GFP-HPos- or GFP-HNeu-transfected cells (24 h stv) and cells additionally incubated 24 h with OA (24 h OA) were fractionated in sucrose density gradients. The distribution of the peptides in the gradients was analyzed by Western blotting with anti-GFP antibodies. Each panel shown represents a separate gradient. The figure also includes representative fractionations in separate gradients of an ER resident protein (Sec61) and a LD protein (Plin2) detected with specific antibodies. (C–F) Distribution of GFP-HNeu and GFP-HPos in starved cells (C and D) or OA-loaded cells (E and F). Bottom panels show high-magnification areas selected from the corresponding panels on top. Arrows in D indicate pre-LDs. Bars: (top) 20 μm; (bottom) 2 μm.

the ER into LDs (Ingelmo-Torres et al., 2009). The signal includes the hydrophobic residues for initial association with the ER, and a sequence enriched in positive amino acids for subsequent targeting into LDs. One class of proteins with endogenous sorting signals of this type are caveolins (Pol et al., 2004), scaffolding molecules that organize specific lipids in different membranes (Bosch et al., 2011) and are required for efficient LD formation (Fernández-Rojo et al., 2012). However, caveolins dynamically associate with LDs and traffic between the ER, LDs, the Golgi complex, endosomes, and the plasma membrane (Pol et al., 2005; Le Lay et al., 2006). A second group of proteins interacting with LDs by hydrophobic domains includes the methyl transferases ALDI, AAM-B, and Erg6. In contrast to caveolins, these proteins shift exclusively between the ER and LDs (Turró et al., 2006; Zehmer et al., 2008; Jacquier et al., 2011). Because such endogenous proteins potentially have additional interactions and functions, we have generated here a minimal model peptide by fusion of the hydrophobic domain of ALDI in order to anchor the peptide to the ER, and the LD targeting signal of caveolin-1, for sorting the peptide within the ER into LDs. This model peptide has a high affinity for LDs and has been used as a marker for LDs and related domains.

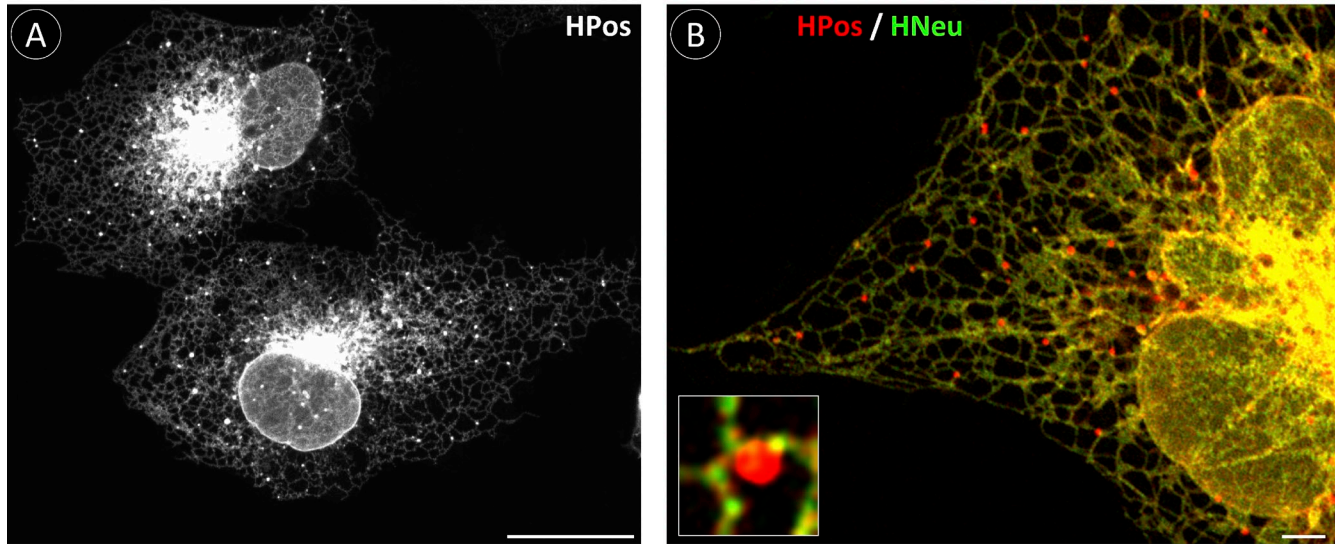
Results

HPos but not HNeu is transported from the ER into LDs after lipid loading

A model peptide (HPos) was generated by fusion of the hydrophobic domain of ALDI with the last 20 residues of caveolin-1 (Fig. 1 A). This caveolin-1 sequence has an isoelectric point of 9.0 and targets caveolin-1 to LDs (Ingelmo-Torres et al., 2009). As a negative control, we mutated to glycines the three positive residues in the positive sequence (Fig. 1 A, bold letters). The resulting peptide (HNeu) accumulates on the ER but is excluded from LDs (Fig. 1). The peptides were N-terminally tagged with fluorescent molecules (GFP or orange fluorescent protein [OPF]). For these microscopy-based studies, we selected COS-1 cells, commonly used to study trafficking of proteins within the ER (Lippincott-Schwartz et al., 2001).

Initially, cells were transfected with GFP-HPos or GFP-HNeu for 24 h in the absence of serum to reduce extracellular lipids and LDs (referred to as starvation). After starvation, cells were fractionated in sucrose density gradients, and there was no visible LD fraction (Fig. 1 B and Nile red in Fig. 8 G). HPos and HNeu were present in the same fraction as the endogenous ER marker Sec61. Endogenous Plin2 was in the bottom of the

HPos accumulation and HNeu exclusion in emerging LDs



LD biogenesis after HPos expression

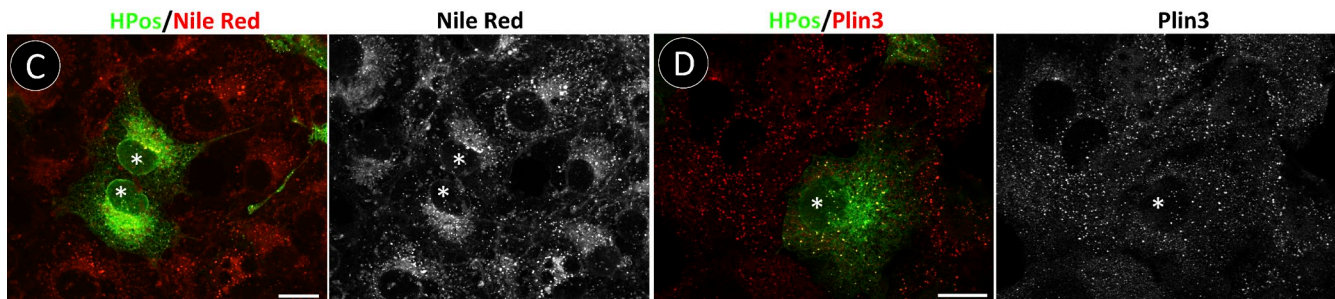


Figure 2. Segregation of HPos into LD after lipid arrival. (A) Starved GFP-HPos–transfected cells were treated with OA for 7.5 min and analyzed by microscopy. (B) Starved GFP-HPos– and GFP-HNeu–cotransfected cells were loaded with OA for 7.5 min and analyzed by microscopy. The inset shows a high-magnification detail of an emerging LD. (C and D) Starved GFP-HPos–transfected cells were loaded with OA for 30 min. The distribution of neutral lipids was detected with Nile red (red in C), and the distribution of endogenous Plin3 was detected with antibodies (red in D). Asterisks indicate transfected cells. Bars: (A, C, and D) 20 μm ; (B, main panel) 2 μm ; (B, inset) 0.5 μm .

gradient, which is consistent with a cytosolic distribution in the absence of LDs. Confocal microscopy confirmed that the peptides accumulated in the nuclear envelope, in central ER sheet-like structures, and in tubules arranged in triple junction polygons forming the branching ER network (Fig. 1, C and D). Electron microscopy analysis confirmed that both markers were completely restricted to the ER (unpublished data). Identical results were obtained when transfected cells were incubated for 24 h in a medium containing 5% of a delipidated FCS (unpublished data).

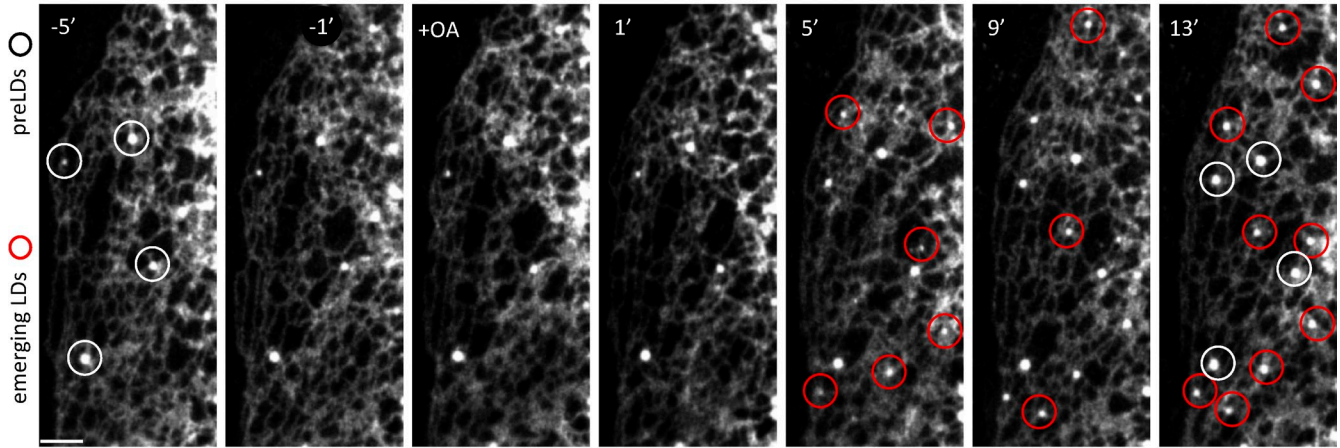
Next, starved HPos- and HNeu-transfected cells were treated for 24 h with 175 $\mu\text{g}/\text{ml}$ of oleic acid (OA) to induce LD formation. The fractionation demonstrated the existence of a LD fraction, enriched for Plin2 and HPos but not for HNeu (Fig. 1 B). Confocal microscopy confirmed that HPos was on LDs (Fig. 1 F) and that HNeu remained in the ER (Fig. 1 E). Thus, HPos follows an OA-promoted transport pathway between the ER and LDs. In addition to being found in the ER tubules of the starved cells, HPos, but not HNeu, was found in small punctate structures apparently connected to the ER (Fig. 1 D, arrows) even though mature LDs were not visible in that cell.

Lipid arrival promotes rapid segregation of HPos within the ER into LDs

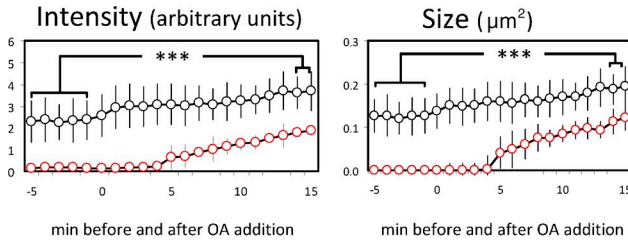
To investigate the LD nucleation sites, we incubated starved HPos-transfected cells with OA for short times. After 7.5 min, HPos had already accumulated in rounded structures consistently connected to the ER (Fig. 2 A). In cotransfected cells, GFP-HPos and GFP-HNeu did not colocalize in these structures (Fig. 2 B), which suggests that they are early LDs. Critically, HPos did not modify the initial stages of LD formation. When starved cells were loaded with OA for 30 min, formation of Nile red–positive LDs was indistinguishable between non-transfected and transfected cells (Fig. 2 C). Further, HPos did not modify the recruitment of endogenous proteins, such as Plin3, in the newly-formed LDs (Fig. 2 D).

We next examined the process with higher temporal resolution using time-lapse confocal microscopy. In these experiments, starved HPos-transfected cells were additionally treated with cycloheximide to reduce the pool of newly synthesized protein, and cells were selected for the labeling of well-defined ER elements. As described above, several HPos-positive structures were present before OA addition (Fig. 3 A, white circles

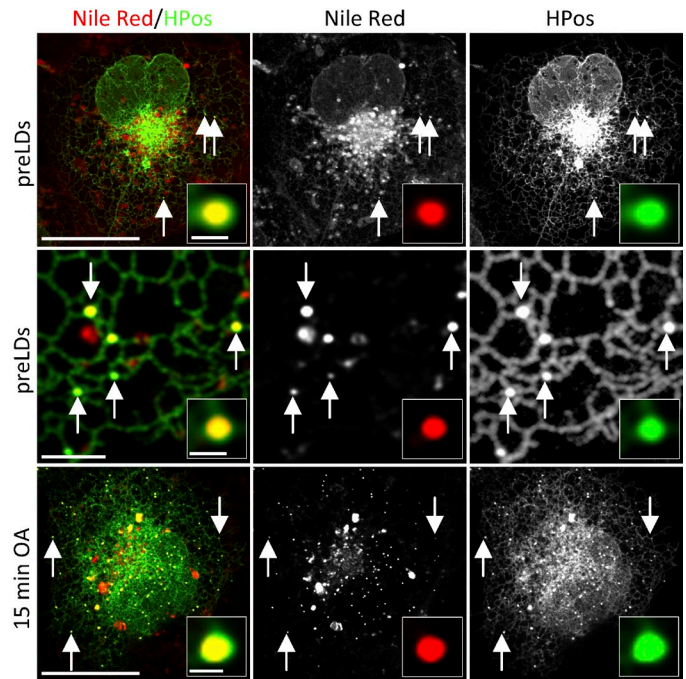
A Dynamics of HPos incorporation into emerging LDs (video microscopy)



B HPos incorporation in LDs (video microscopy)



D Neutral lipid accumulation in pre- and emerging LDs



C Size and number of emerging LDs

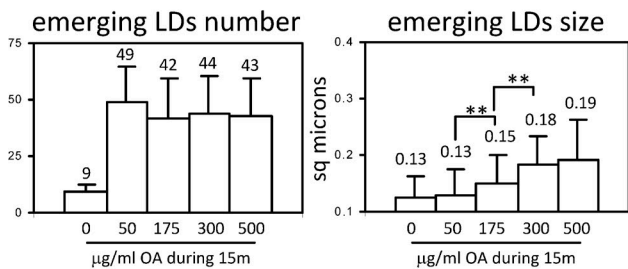


Figure 3. Dynamics of HPos incorporation into emerging LDs. (A) Starved GFP-HPos–transfected cells were analyzed by video microscopy (Video 1). Pre-LDs (white circles) were followed for 5 min and then cells were loaded with OA (+OA). Red circles indicate LDs emerging after 5 or 9 min. Bar, 2 μ m. (B) Quantification of HPos fluorescence intensity and size of pre-LDs (black circles) and emerging LDs (red circles) in three independent experiments as in A. (C) Starved GFP-HPos–transfected cells were treated with increasing OA concentrations for 15 min. Cells were fixed and the sizes and numbers of emerging LDs were quantified. **, $P < 0.01$; ***, $P < 0.001$. (D) Starved GFP-HPos–transfected cells (top) were loaded with OA for 15 min (bottom). Cells were fixed, neutral lipids were detected with Nile red (red), and the cells were analyzed by microscopy. Arrows indicate the HPos- and Nile red–positive structures. The insets show high-magnification details of pre-LDs (top and middle) and an emerging LD (bottom) labeled with Nile red. Bars: (top and bottom) 20 μ m; (middle) 2 μ m; (insets) 0.5 μ m. Error bars indicate the standard deviation of at least 60 structures from three independent experiments.

in -5' panel; and Video 1). These structures were apparently stable in the ER. Because these structures exclude HNeu (see Fig. 8), contain a core of neutral lipids (Fig. 3 D), and were observed before the OA addition, we denote these as “pre-existing LDs” (pre-LDs).

Once OA was added (+OA in Fig. 3 A and Video 1), additional HPos-positive structures appeared in ~5–7 min (Fig. 3 A, red circles), and we denote these as “emerging LDs.” The treatment with OA caused accumulation of HPos into the puncta. For pre-LDs, HPos was incorporated within 30–60 s (Fig. 3 B,

black circles), and for emerging LDs there was a roughly 5-min delay between OA addition and visible HPos accumulation (Fig. 3 B, red circles). At the end of the video, 15 min after OA addition, Nile red labeled the emerging LDs (Fig. 3 D, bottom), which indicates that these sites are bona fide LDs. Similar to caveolins recruited to LDs from the ER (Pol et al., 2004), but in contrast to Plin2 (Soni et al., 2009), preincubation with brefeldin A for 15 min before the addition of OA did not modify the accumulation of HPos in emerging LDs (unpublished data), which suggests that this peptide is not transported via vesicular

trafficking. Thus, the results confirm that HPos shifts from the ER into nascent LDs.

The assembly of lipoproteins occurs in defined nucleation ER sites, but it has been proposed that LD assembly initiates spontaneously, simply by accumulation of neutral lipids in the ER (Sturley and Hussain, 2012). If this model is correct, more lipid arrival should promote more spontaneous LD nucleation and more emerging LDs. To test this hypothesis, starved HPos-transfected cells were treated for 15 min with different OA concentrations, and the number and sizes of emerging LDs were quantified. Interestingly, consistent with the existence of a limiting step in LD assembly, lipid concentration determined the rate of growth of emerging LDs but not the number of emerging structures, which was relatively constant (Fig. 3 C).

Dynamics of lipid incorporation into pre-LDs and emerging LDs

We next determined whether lipids were incorporating into pre- and emerging LDs coincident with the HPos accumulation. To visualize lipid dynamics, we used a BODIPY-tagged fatty acid (FA-BODIPY). This FA-BODIPY is a convenient tool because it can be followed in living cells and is esterified (Carten et al., 2011). In COS cells, esterification was observed early after lipid addition and was highly reduced with Triacsin C (acyl-CoA synthetases inhibitor, Fig. 4 E), which suggests lipid metabolism. Further, the signal corresponding to the esterified fatty acid was lost after saponification of the samples (not depicted).

Next, starved OFP-HPos-transfected cells were loaded with OA and the FA-BODIPY ($t = 0$) and visualized via time-lapse microscopy (Videos 2 and 3). After just 10–30 s, the lipid accumulated within pre-LDs (Fig. 4 A, white circles). Emerging LDs appeared 5–7 min after OA addition (Fig. 4 A, red circles; and Video 3). In this image, two such emerging LDs are clearly visible at $t = 10$ min, and by $t = 13$ one of them has clearly started to accumulate FA-BODIPY (Fig. 4 A, blue arrow). By quantifying FA-BODIPY incorporation in multiple pre- and emerging LDs (Fig. 4 D), we observed that significant lipid packaging was evident within seconds in pre-LDs (Fig. 4 B), but for emerging LDs there was a 2.3 ± 0.9 min mean delay between initial formation of LDs and FA-BODIPY accumulation (Fig. 4 C). After formation, the rate of lipid incorporation into emerging LDs was very similar to pre-LDs (Fig. 4 D). In conclusion, both pre-LDs and emerging LDs are bona fide sites of lipid accumulation but with different kinetics.

Dynamics of protein incorporation into pre-LDs and emerging LDs

HPos is recruited to nascent LDs before lipid accumulation becomes evident, and thus provides a convenient marker to characterize initial stages of LD formation. We therefore used HPos as a temporal marker to examine the relative arrival of other proteins involved in the process such as Plin2, Plin3, ACSL3, and DGAT2. A current model suggests that nascent LDs are coated with Plin3, which is progressively replaced by Plin2 (Wolins et al., 2005). A fragment of the acyl-CoA synthetase 3

(ACSL3) was recently described in nascent LDs (Poppelreuther et al., 2012). Finally, although the presence of diacylglycerol acyltransferase 2 (DGAT2) on LDs is controversial, the activity of DGAT2 is required to form triglycerides (Kuerschner et al., 2008; Stone et al., 2009; Brasaemle and Wolins, 2012). Thus, these four proteins were tagged and cotransfected with HPos in starved cells. Emerging LDs were promoted with OA for 7.5, 15, or 30 min, and colocalization between HPos and the markers was quantified in fixed cells.

Interestingly, DGAT2 did not colocalize with HPos in pre-LDs or emerging LDs (Fig. 5, A and B), which suggests that neutral lipid generation does not necessarily occur at the sites of storage. Plin2 and Plin3 demonstrated a low colocalization with pre-LDs but progressively accumulated in emerging LDs. After 7.5 min, ~50% of the emerging LDs contained Plin2 and Plin3. Recruitment of these proteins progressively increased with longer incubations. In agreement with previous studies (Wolins et al., 2005), Plin3 demonstrated a more rapid accumulation in emerging LDs than Plin2 (Fig. 5, A and B). A similar partial colocalization was observed between HPos and endogenous Plin2 and Plin3 (Fig. S1). Interestingly, the myc-tagged ACSL3 demonstrated an almost complete colocalization with HPos on pre-LDs and emerging LDs (Fig. 5, A and B; and Fig. S1), which suggests that ACSL3 is recruited earlier to LDs. Before and after OA, Plin3 additionally accumulated in rounded structures that excluded ACSL3 but that were not LDs as determined by the absence of BODIPY 493/503, a neutral lipid dye (Fig. S1 E).

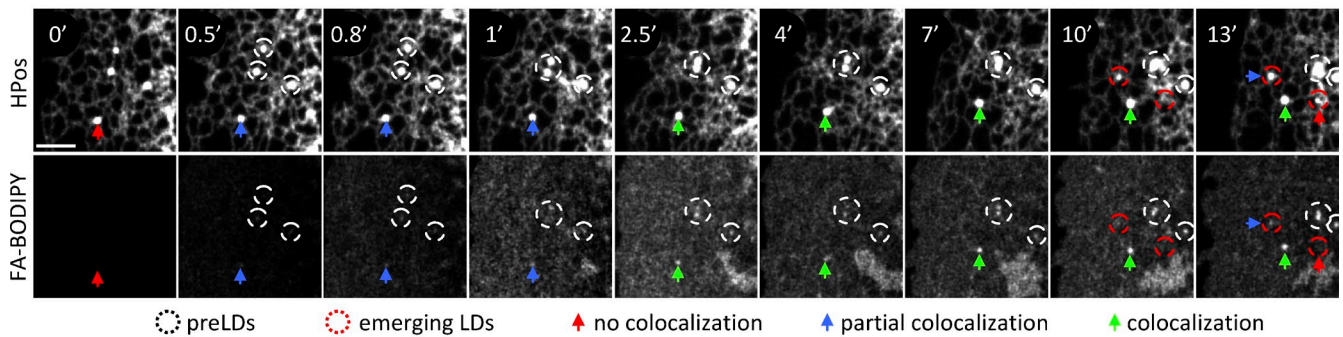
To examine whether the increased colocalization with HPos reflects the progressive incorporation of the markers into emerging LDs, we studied GFP-Plin2 incorporation via time-lapse microscopy. Thus, OFP-HPos and GFP-Plin2 were co-expressed in starved cells. After 5–7 min of OA addition, HPos-positive emerging LDs were formed. Immediately after formation these structures excluded Plin2 (Fig. 5 C). However, Plin2 was recruited to emerging LDs after a mean time of 4.5 ± 1.8 min, which is consistent with the hypothesis that LD assembly follows a coordinated sequence of protein recruitments (Wolins et al., 2005).

Endogenous ACSL3 is on pre-LDs and emerging LDs

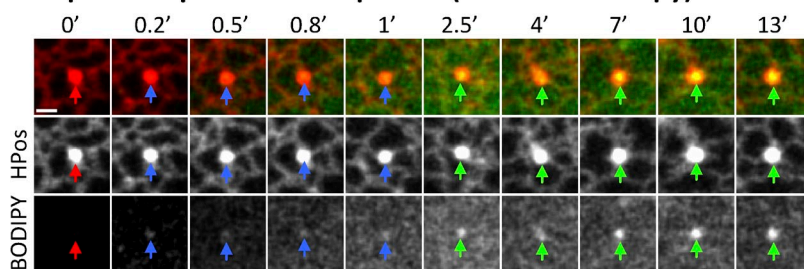
Initially, ACSL3 was defined as an abundant LD protein in two proteomic screenings (Brasaemle et al., 2004; Fujimoto et al., 2004). Subsequently, biochemical analysis suggested that ACSL3 is the most abundant acyl-CoA synthetase long-chain family (ACSL) on LDs, and the role of this enzyme in LD formation was suggested (Fujimoto et al., 2007). In agreement with this proposal, inhibition of the ACSLs activity with Triacsin C blocks the fatty acid-induced formation of LDs (Brasaemle et al., 2000; Fujimoto et al., 2007; Herms et al., 2013). Recently, as commented above, a fragment of ACSL3 was shown in nascent LDs (Poppelreuther et al., 2012). Now, we have demonstrated that full-length ACSL3 is also early to arrive to emerging LD.

Further, antibodies against ACSL3 demonstrated that the endogenous enzyme (endACSL3) also accumulates in pre-LDs

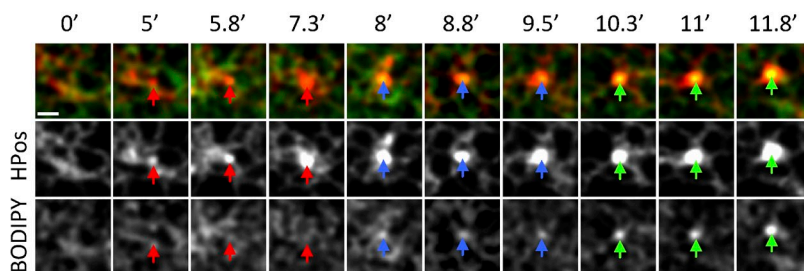
A Dynamics of lipid incorporation into preLDs and emerging LDs (video microscopy)



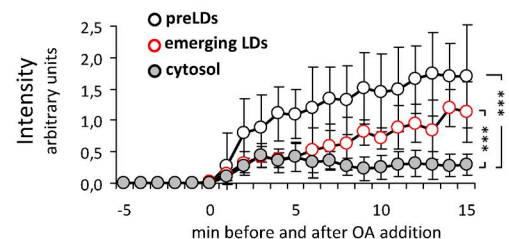
B Lipid incorporation into preLDs (video microscopy)



C Lipid incorporation into emerging LDs (video microscopy)



D FA-BODIPY incorporation into LDs



E FA-BODIPY esterification (TLC)

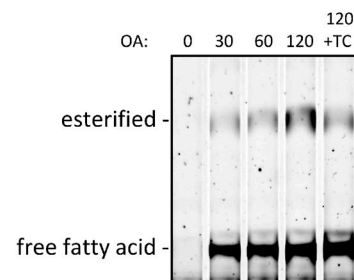


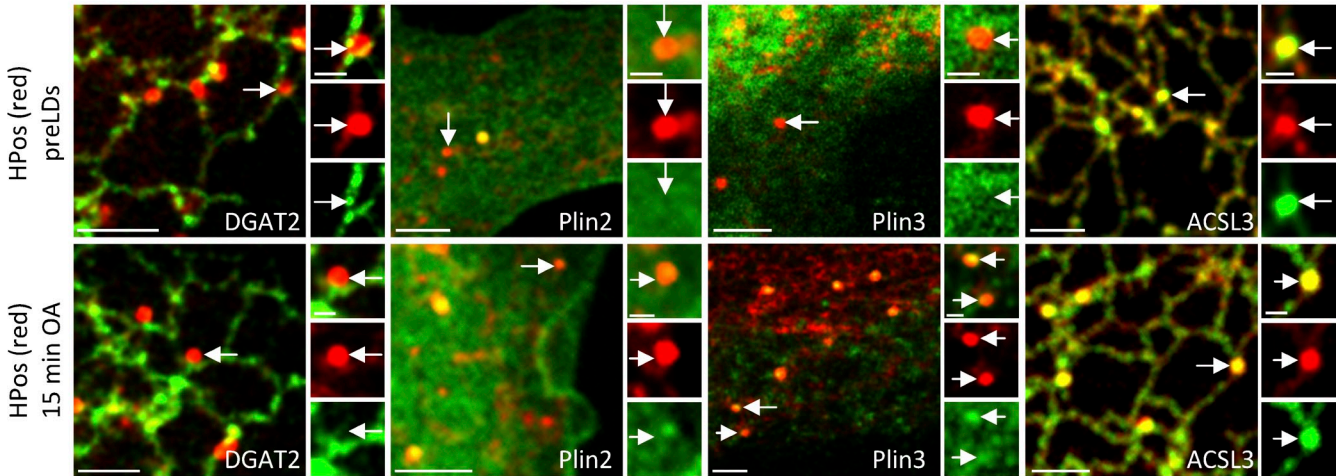
Figure 4. Dynamics of lipid incorporation into pre- and emerging LDs. (A) Starved GFP-HPos-transfected cells (top) were treated with OA and FA-BODIPY (bottom) and followed after 15 min by video microscopy (Video 2). Blue and green arrows indicate FA-BODIPY accumulation in pre-LDs. White circles indicate pre-LDs, and red circles emerging LDs. Arrows indicate a representative pre-LD. The degree of colocalization between HPos and FA-BODIPY at different times is indicated by the color of the arrow; red denotes a lack of colocalization, blue partial colocalization, and green complete colocalization. (B) A high-magnification sequence of lipid incorporation into the pre-LD indicated with a red arrow in the first panel of A (Video 3). The arrows mark the pre-LD selected in A. (C) A high-magnification sequence of lipid incorporation into the emerging LD indicated with a blue arrow in the last panel of A (Video 3). Arrows mark a representative emerging LD. (D) Cells were treated as in A, and the FA-BODIPY intensity in at least 30 pre-LDs (black circles), emerging LDs (red circles), and the cytosol (gray circles) was quantified before and after OA in three independent experiments. Error bars indicate the standard deviation between experiments. ***, $P < 0.001$. (E) Thin-layer chromatography of fluorescent lipids in cells incubated 30, 60, or 120 min with OA and FA-BODIPY or 120 min but in the presence of 10 μ M Triacsin C (TC). Bars: (A) 2 μ m; (B and C) 0.5 μ m.

(Figs. 6 A and S1) and emerging LDs (Figs. 6 D and S1). In addition, colocalization between endACSL3 and HPos revealed the existence of additional pre-LDs in the central regions of starved cells that were not previously detected by accumulation of HPos (Fig. 6 A, blue arrows). The complete redistribution of ACSL3 from the ER into LDs was confirmed by fractionation of starved and OA-treated cells (Fig. 6 B) and by immunofluorescence microscopy (Fig. 6 C). The ACSL3 protein levels were slightly but consistently higher in starved cells than cells treated for 24 h with OA (Fig. 6 E). Altogether, these results established that endACSL3 is either recruited early into emerging LDs or, alternatively, that ACSL3 plays a role in LD assembly.

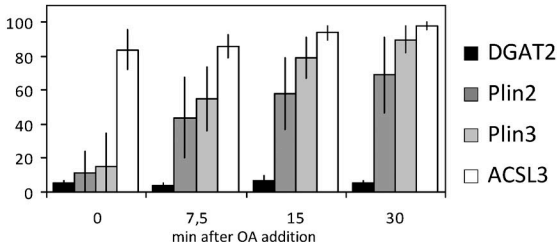
ACSL3 regulates biogenesis, accumulation, copy number, and size of LDs

We quantified the number of pre- and emerging LDs in HPos-transfected cells with reduced or increased levels of ACSL3 (Fig. 7 A). The number of pre-LDs was significantly reduced in starved cells with lowered levels of ACSL3 (achieved by siRNA) and increased in cells cotransfected with the myc-ACSL3 (Fig. 7 B). Further, the number of emerging LDs was significantly reduced when the siRNA-treated cells were incubated with OA (Fig. 7 B, red bars) but increased in the cells cotransfected with the myc-ACSL3 (black bars). After 60 min, mature LDs, with a ring-like distribution of HPos, accumulated in more central regions of the cells. These larger LDs, which

A Dynamics of LD protein incorporation into preLDs and emerging LDs (microscopy)



B % colocalization of LD proteins with HPos



C Plin2 incorporation into emerging LDs (video microscopy)

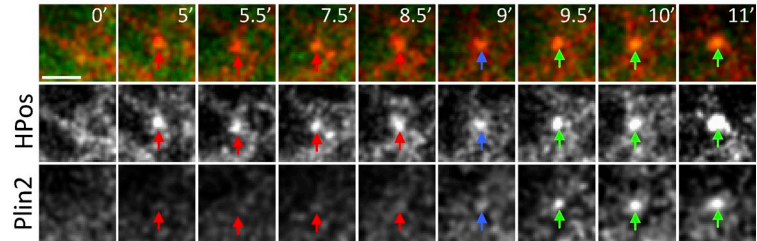
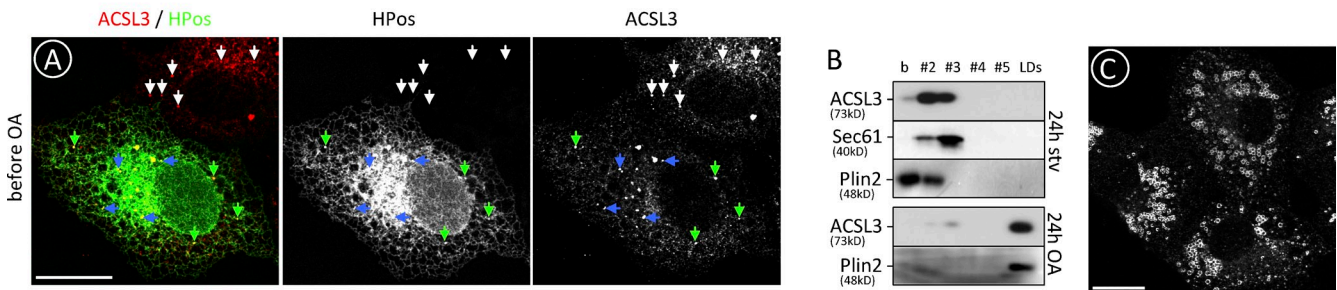
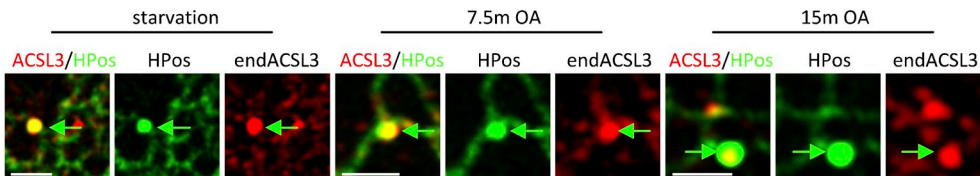


Figure 5. **Dynamics of protein incorporation into emerging LDs.** (A and B) Starved cells (top) cotransfected with GFP-HPos and tagged forms of DGAT2, Plin2, Plin3, and ACSL3 (green), were additionally treated with OA for 7.5, 15 (bottom), or 30 min and analyzed by microscopy. Arrows indicate the structures selected for the high-magnification panels. Bars: (main panels) 2 μ m; (insets) 0.5 μ m. (B) The percentage of HPos-positive pre- and emerging LDs that accumulated the cotransfected proteins. Error bars indicate the standard deviation of three independent experiments. (C) Starved GFP-HPos and GFP-Plin2 cotransfected cells were loaded with OA and followed for 15 min by video microscopy. After formation (t = 0), HPos-positive emerging LDs require a mean time of 4.5 ± 1.8 min to be recognized by Plin2 (blue and green arrows). Arrows mark a representative emerging LD, and the color of the arrow indicates the degree of colocalization between HPos and Plin2. Bar, 1 μ m.

Endogenous ACSL3 distributes between the ER, preLDs and LDs



D Endogenous ACSL3 accumulates in preLDs and emerging LDs



E ACSL3 levels

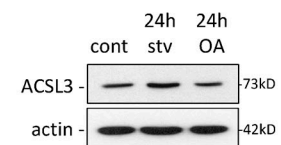
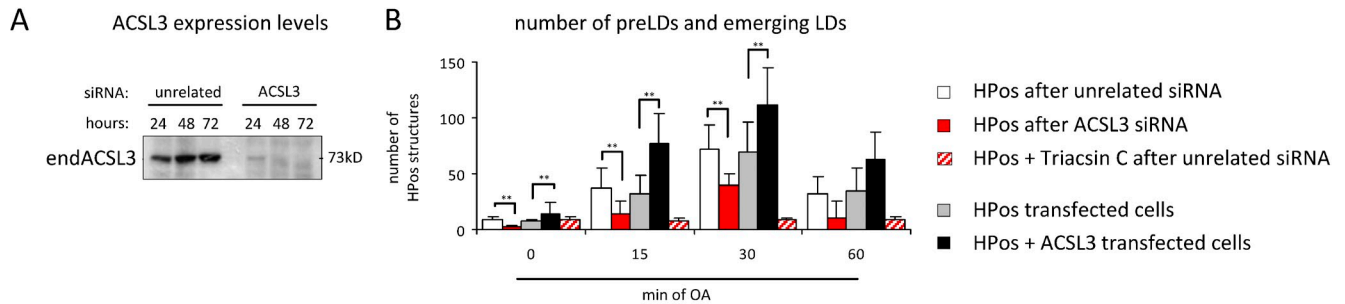
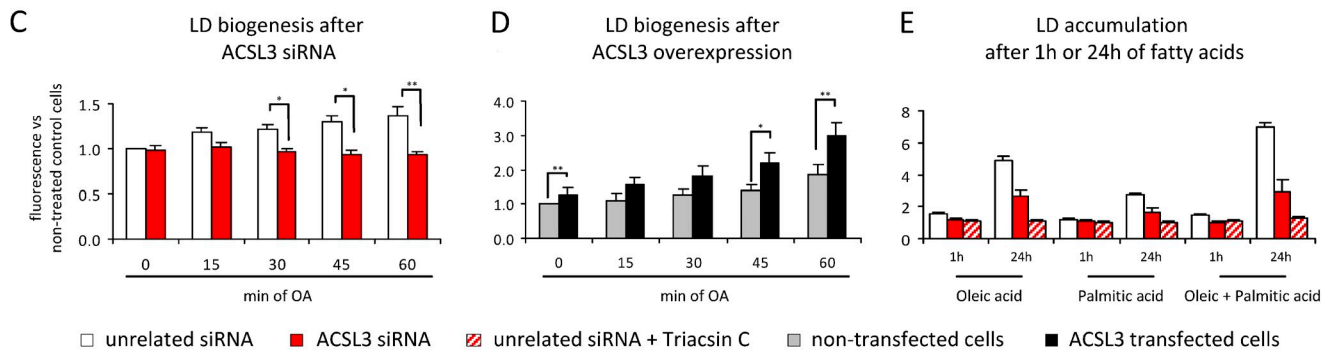


Figure 6. **Endogenous ACSL3 colocalize with HPos in pre- and emerging LDs.** (A) Starved GFP-HPos-transfected cells were fixed and labeled with an antibody for ACSL3. Green arrows indicate colocalization, white arrows indicate equivalent structures to pre-LDs found in nontransfected cells, and blue arrows indicate pre-LDs in central regions of the cell. (B) Distribution of ACSL3, Sec61, and Plin2 in starved cells (top) and cells additionally treated with OA for 24 h (bottom) and fractionated in sucrose density gradients. (C) Distribution of ACSL3 in cells treated with OA for 24 h. (D) Starved GFP-HPos-transfected cells were additionally treated with OA for 7.5 or 15 min, and cells were fixed and labeled with the ACSL3 antibody. Green arrows indicate colocalization. (E) ACSL3 protein levels detected by Western blotting of homogenates of normal cells (control), starved cells (24 h stv), and cells additionally treated with OA for 24 h (24 h OA). Bars: (A and C) 20 μ m; (D) 1 μ m.

ACSL3 regulates the number of preLDs and emerging LDs (microscopy)



ACSL3 regulates neutral lipid accumulation (flow cytometry)



ACSL3 regulates the copy number and size of mature LDs (microscopy)

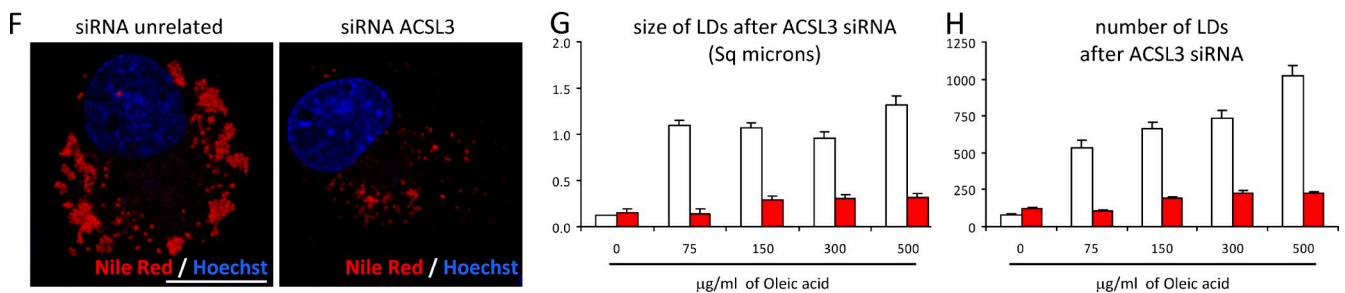


Figure 7. ACSL3 regulates LD biogenesis and neutral lipid accumulation. (A) After transfection with the ACSL3 siRNA or an unrelated siRNA, the protein levels of ACSL3 were determined by Western blotting. (B) The number of HPos-positive structures in starved cells (pre-LDs) or in cells additionally incubated with OA (emerging LDs) was quantified. Red and white bars correspond to cells treated for 24 h with the ACSL3 siRNA (red bars) or the unrelated siRNA (white bars), transfected with HPos, and additionally starved for 24 h. In some of these experiments Triacsin C (slashed bars) was present during starvation and loading. Gray and black bars correspond to cells transfected with HPos (gray bars) or cotransfected with HPos and myc-ACSL3 (black bars) and starved for an additional 24 h. (C–E) Neutral lipids were quantified by flow cytometry after starvation or the indicated times of fatty acid addition in cells previously transfected with the ACSL3 siRNA (red bars) or the unrelated siRNA (white bars), nontransfected cells (gray bars), or cells transfected with myc-ACSL3 (black bars). In some experiments cells were additionally incubated with Triacsin C (slashed bars). (F–H) Cells treated as in C were loaded with OA for 12 h and stained with Nile red (red in F) and Hoechst to visualize the nucleus (blue). In these images the size (G) and number (H) of LDs were quantified. Bar, 20 μ m. Error bars indicate the standard deviation of three independent experiments. *, $P < 0.05$; **, $P < 0.01$.

were not considered in this initial analysis of emerging LDs, coexisted with peripheral and small HPos structures, suggesting that new rounds of emerging LDs occur after 30 min of the lipid arrival (an example is shown in Fig. 1 F).

To demonstrate that the number of pre- and emerging LDs correlates with the early storage of neutral lipids occurring in these structures (Fig. 3 D), starved cells transfected with the siRNA for ACSL3 or the myc-ACSL3 were loaded with OA and labeled with neutral lipid dyes, then cellular fluorescence was measured via flow cytometry (Herms et al., 2013). Accumulation of neutral lipids was completely inhibited in the

absence of ACSL3 (Fig. 7 C) but accelerated by overexpression of myc-ACSL3 (Fig. 7 D). Decreased LD biogenesis in the absence of ACSL3 was also observed when LDs were promoted with palmitic acid (Fig. 7 E). Further, lack of ACSL3 completely inhibited the incorporation of a radiolabeled OA into triacylglycerols, as measured by thin layer chromatography (unpublished data).

Changes in LD assembly should also determine long-term neutral lipid accumulation. Thus, cells transfected with the ACSL3 siRNA or with an unrelated siRNA were treated for 12 h with increasing OA concentrations. LDs were labeled with Nile

red, and final LD copy number and size were quantified in microscopy images (Fig. 7 F). In control cells, LD size was relatively constant over a broad range of OA concentrations (Fig. 7 G, white bars), while the number of LDs increased as a function of lipid concentration (Fig. 7 H, white bars). The lack of ACSL3 drastically reduced both the size and the number of LDs (Fig. 7, G and H, red bars). The flow cytometry analysis also demonstrated that cells with lowered levels of ACSL3 accumulated fewer LDs when treated for 24 h with OA or palmitic acid (Fig. 7 E). Further, the inhibition of LD formation after the ACSL3 siRNA was rescued by an ectopically expressed siRNA-resistant ACSL3 (Fig. S3, D and E). In addition, ACSL3 also determined the LD content of hepatic cells (Fig. S4).

To analyze whether the enzymatic activity of ACSL3 determines LD formation, cells were loaded with OA, but in the presence of Triacsin C, an inhibitor of ACSL1, ACSL3, and ACSL4 (Soupe and Kuypers, 2008). LD nucleation and accumulation were almost completely inhibited by Triacsin C (Fig. 7, B and E, slashed bars). A quantitative RT-PCR (qRT-PCR) analysis demonstrated that ACSL1 and ACSL4 are also expressed in COS cells. When normalized to the ACSL3 expression, ACSL4 was the most abundant member ($\times 1.2$), and ACSL1 demonstrated a lower but consistent expression ($\times 0.2$). However, siRNAs for these ACSLs did not affect LD accumulation (Fig. S2, A–E). Further, when GFP-tagged forms of these ACSLs were expressed to identical levels, only the GFP-ACSL3 increased LD formation and accumulation (Fig. S2, F–H), which suggests that ACSL3 is the member involved in LD biogenesis. Interestingly, a transfected GFP-ACSL3 without the Gate domain (ACSL3 Δ gate), and thus with no enzymatic activity (Fig. S3), also accelerated the early storage of neutral lipids and partially increased LD accumulation (Fig. S3, F and G). This lends support to the hypothesis that although the enzymatic activity of ACSL3 is required for LD nucleation and expansion, other properties of the enzyme also cooperate during the process.

Pre-LDs are stable LDs in restricted ER microdomains

Finally, we wanted to characterize the pre-LDs, and hypothesized that these structures are LDs stably assembled in ER membranes and specialized in the rapid packaging of arriving lipids. As expected, pre-LDs accumulated different HPos peptides (OFP-HPos and GFP-Hyd-ER3; Ingelmo-Torres et al., 2009) but completely excluded HNeu (Fig. 8, B and A). However, pre-LDs were only partially recognized by ectopically expressed or endogenous Plin proteins (Fig. 8 C and Fig. S1). First, to address if pre-LDs are different from the rest of the ER, we investigated the mobility of HPos and analyzed protein dynamics by FRAP. Most ER-localized proteins are highly mobile (Lippincott-Schwartz et al., 2001), and indeed when GFP-HPos in tubules was photobleached demonstrated a mobile fraction of 99% in 20 s (Fig. 8 D, white circles). In striking contrast, when the protein on pre-LDs was photobleached, the mobile fraction was $\sim 16\%$ in 20 s ($t_{1/2} = 62.8$ s; Fig. 8 D, red circles). Likely reflecting the smaller size of the peptide, these kinetics are slightly more rapid but consistent with other LD

proteins such as GFP-Dga1 ($t_{1/2} = 82.9$ s) proposed to laterally move between the ER and LDs (Jacquier et al., 2011).

Pre-LDs could be mature LDs assembled before the starvation and incompletely metabolized in a lipid-depleted environment. However, pre-LDs were only partially recognized by Plin2 and Plin3 (Figs. 5 and S1), which suggests that this is not the case. Further, pre-LDs were not formed during the starvation period, as the number of these domains was not reduced by Triacsin C (Fig. 7 B). Thus, one possibility is that pre-LDs are actually LDs that were forming before the time that cells were submitted to lipid deprivation, and thus equivalent structures to the emerging LDs that are only partially recognized by Plin proteins (Fig. 5, A and B; and Fig. S1). However, such a model would require that in the absence of a lipid supply, emerging LDs should be stable in the ER.

We therefore treated starved cells for 10 min with OA in order to promote emerging LDs, and then cells were resubmitted to starvation for 16 h to test whether these LDs were stable in the absence of extracellular lipids. Flow cytometry analysis demonstrated that the accumulation of lipids promoted by the lipid pulse was stable during the second starvation period (Fig. 8 E). In contrast, mature LDs formed with OA for 24 h and submitted to an identical starvation were metabolized (Fig. 8 F). The microscopy analysis of cells stained with Nile red revealed that, in contrast to starved cells (Fig. 8 G), cells submitted to the single pulse of lipids accumulated numerous LDs (Fig. 8 H) and that the lipid accumulation persisted after the second starvation (Fig. 8 I). The stability of these early formed LDs was confirmed in other cell lines such as 3T3-L1 and mouse embryonic fibroblasts (unpublished data). These structures excluded endogenous Plin3 (not depicted) and accumulated endogenous ACSL3 (Fig. 8 J).

We then characterized the morphology of pre-LDs by electron microscopy. Cells were treated as indicated above and processed with no primary fixative and a very quick nonperturbing freeze substitution protocol. We found that after the second starvation, cells accumulated numerous electron lucent structures that were not present in starved cells (Fig. 9, A and B). These pre-LDs were often close to the ER, clearly surrounded by a monolayer, and demonstrated a very consistent size (257.6 ± 31 nm), as expected from a synchronized process of biogenesis (Fig. 3). In some cases a likely interaction between the LDs and the ER (Fig. 9 C, arrows) and with other LDs (Fig. 9 D, arrows) was observed.

To get further structural details, we used electron tomography (Videos 4 and 5). Cells were treated and processed as above and the specimen (300 nm thick) was tilted $\pm 60^\circ$ in both axes, taking images every 1 or 2° (Nixon et al., 2009). With this 3D view we did not observe any completely spherical LDs (Fig. 9 E), which suggests that pre-LDs may be relatively flat structures (Figs. 9 A and 10). Tomography clearly illustrated that pre-LDs are surrounded by a monolayer, which was especially obvious when compared with the ER bilayer distinguished by the presence of electron-dense ribosomes (Fig. 9 F and Video 4). Interestingly, because tomography allows visualization of the organelle at different levels, we observed that almost all the pre-LDs showed at least one contact with the ER,

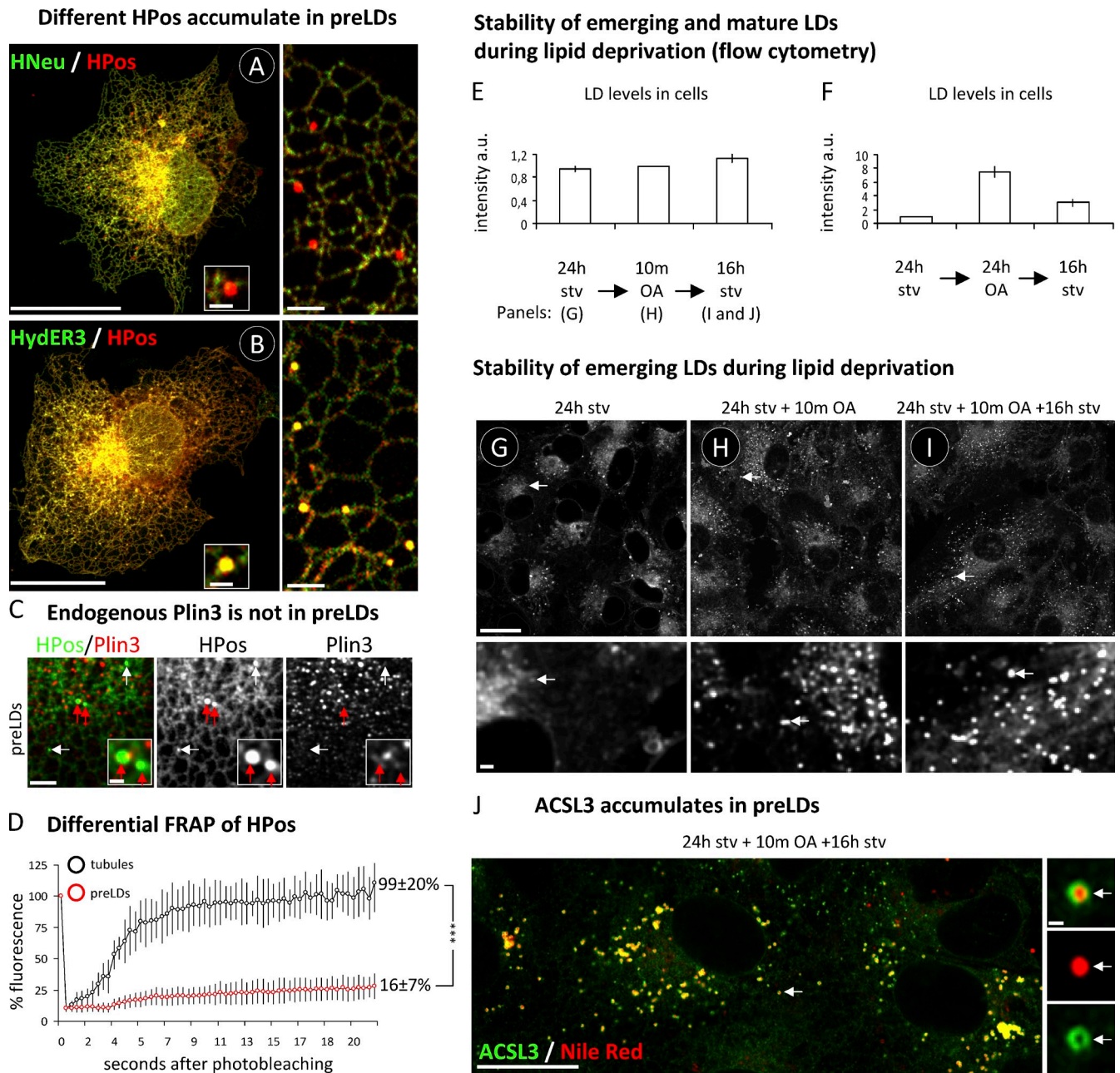


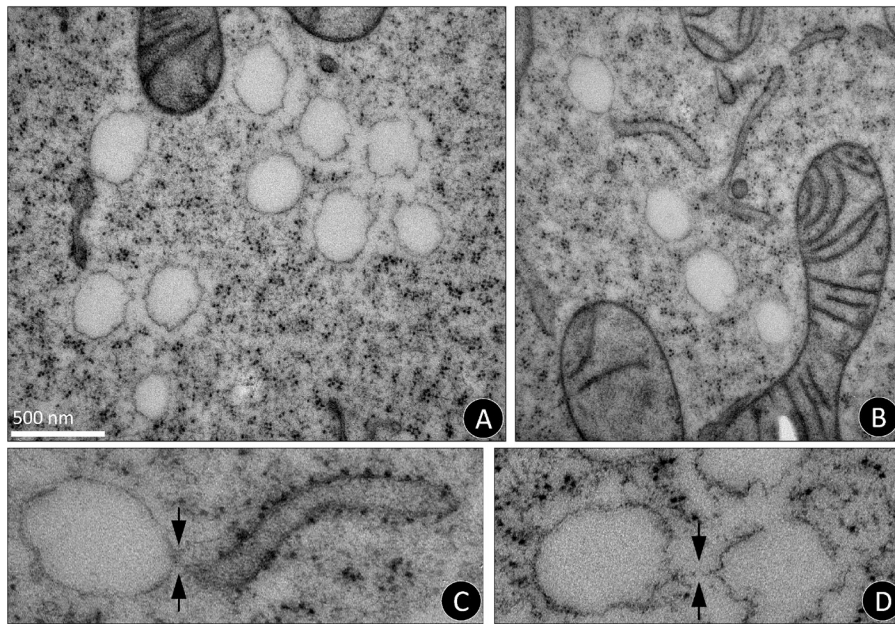
Figure 8. Pre-LDs are restricted and stable ER microdomains. (A and B) Starved cells cotransfected with GFP-HPos and GFP-HNNeu (A) or GFP-HPos and GFP-HydER3 (an HPos peptide with the positive sequence of ALDI; B) were fixed and analyzed by confocal microscopy. Bars: (left) 25 μ m; (right) 2 μ m; (insets) 0.5 μ m. (C) Starved GFP-HPos-transfected cells were fixed, and distribution of endogenous Plin3 was analyzed with a specific antibody (red). Red arrows indicate the pre-LDs selected for the high-magnification panel. Bars: (main panels) 2 μ m; (insets) 0.5 μ m. (D) Starved GFP-HPos-transfected cells were photobleached in tubules (black circles) or in pre-LDs (red circles). Fluorescence recovery was quantified. (E and F) Starved cells (stv) were treated for 10 min (E) or 24 h (F) with OA and then submitted to a second starvation for an additional 16 h (16 h stv). Neutral lipids were labeled with Nile red and quantified by flow cytometry. (G–I) Cells treated as in E were stained with Nile red and analyzed by microscopy. Bars: (top) 25 μ m; (bottom) 2 μ m. (J) Cells submitted to the second starvation period as in E (16 h stv) were fixed and labeled with Nile red (red) and ACSL3 antibody (green). Bars (main panel) 25 μ m; (insets) 0.5 μ m. Error bars indicate the standard deviation of five (D) or three (E and F) independent experiments.

and in some cases a likely continuity between the membranes of both organelles was observed (Fig. 9 F, arrows). In addition, pre-LDs were apparently connected to neighboring LDs by a continuous monolayer (Fig. 9 G, arrows; and Video 4), perhaps suggesting that those nearby pre-LDs were formed in the same ER tubule. Some pre-LDs demonstrated a simultaneous triple connection, for example, with two ER tubules and one LD (Fig. 9 H, arrows).

Discussion

The ER is a continuous and dynamic system of connected membranes organized in different subdomains, including the nuclear envelope, central rough sheet-like structures, and a polygonal network of tubules extending into the cell periphery (Park and Blackstone, 2010). The rough ER participates simultaneously in protein synthesis, quality control, and protein and

preLDs visualized with freeze substitution electron microscopy



preLDs visualized by electron tomography

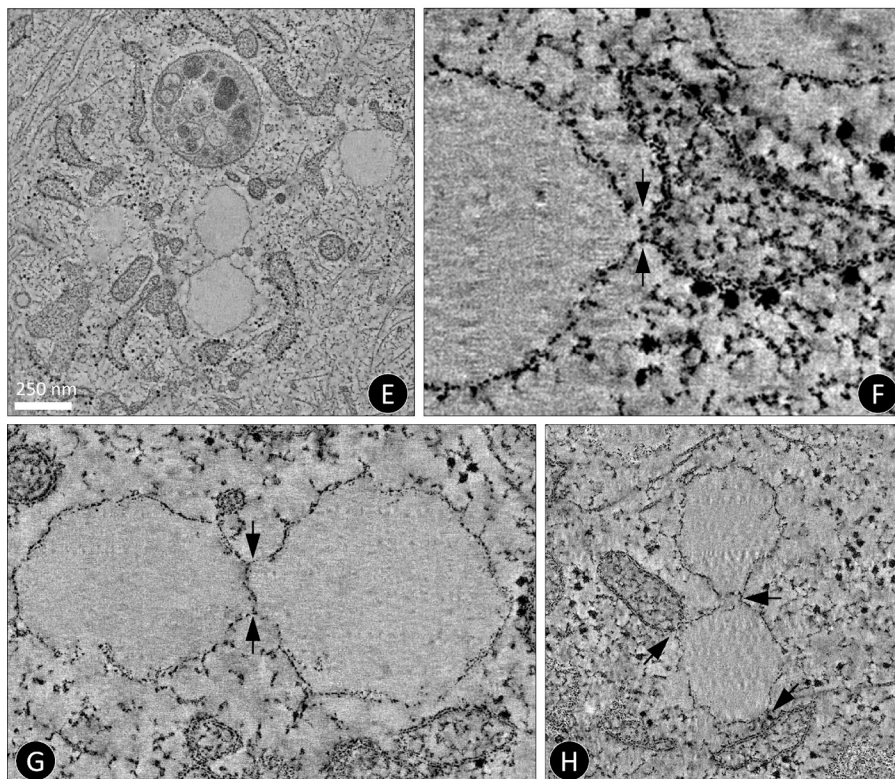


Figure 9. **Ultrastructure of pre-LDs.** Cells submitted to the second starvation period as in Fig. 8 E (16 h stv) were analyzed by electron microscopy (A–D) and electron tomography (E–H). A, B, and E show a general view of the cells. Arrows in C, F, and H indicate possible interactions between the ER and pre-LDs. Arrows in D, G, and H indicate possible interactions between neighboring pre-LDs. For additional details, E and G correspond to the central pre-LD of [Video 4](#), and F corresponds to the central pre-LD in [Video 5](#).

lipid secretion. The tubules specialize in detoxification, lipid synthesis, and interaction with other organelles. Remarkably, although all these ER subdomains and microdomains are contiguous and physically in contact, highly selective yet poorly understood mechanisms must exist to ensure that they are functionally segregated.

Fatty acids and cholesterol are key molecules in many cellular processes ranging from the production of metabolic energy to the regulation of membranes fluidity. However, because

free fatty acids and cholesterol can be toxic, they are rapidly esterified into neutral lipids that accumulate in LDs. In mammalian cells, the ER harbors enzymes required for neutral lipid synthesis (Buhman et al., 2001), which suggests that this organelle is also specialized in lipid storage. However, this ER-generation model has been continuously challenged because sites and mechanisms of LD nucleation remain poorly understood.

Here, with fluorescent peptides that shift between the ER and forming LDs, we observed three early aspects of lipid

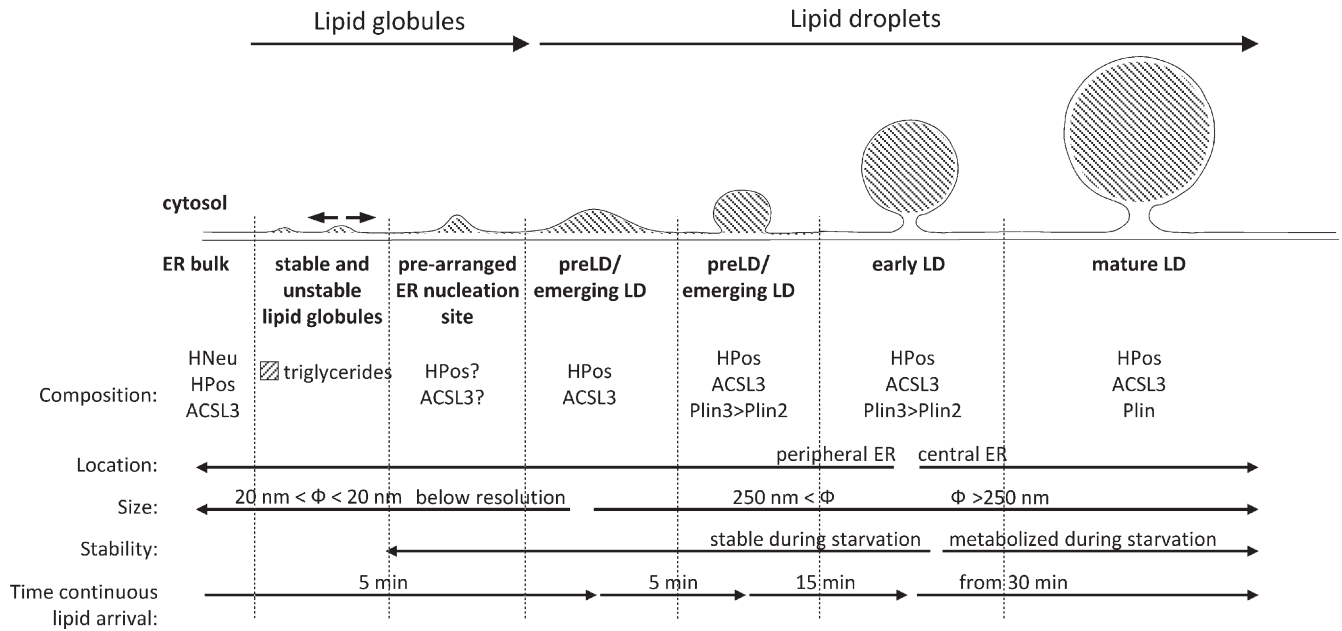


Figure 10. **Model of a self-reinforcing stepwise LD formation.** Continuous lipid arrival promotes the formation of emerging LDs in ~5 min. Initially, newly synthesized neutral lipids can be integrated in the ER membrane. However, addition of new triglycerides to the globule will promote phase separation and the deposition of the globule between the two leaflets of the ER bilayer. These globules produce a transient curvature of the ER membrane or move two-dimensionally within the bilayer, fuse with other globules, and generate curvature of the ER. Proteins with amphipathic α helices, such as HPos or ACSL3, are then attracted to these regions. The stable interaction of these proteins nucleates unstable globules and marks the onset of LD biogenesis. The enrichment of ACSL3 locally generates the acyl-CoA required for LD growth and expansion but also numerous bioactive lipid intermediates. Emerging LDs expand and the lipid intermediates are recognized by Plin proteins. If lipid supply ends, these structures become stable and remain connected to the peripheral ER. If lipid supply persists, emerging LDs increase in size to become early and mature LDs. Early and mature LDs accumulate in the central ER and are metabolized during starvation.

storage. First, arriving lipids are packed in preexisting, or resistant to starvation, LDs. Second, the continuous lipid arrival promotes the formation of a first round of emerging LDs. This assembly is a synchronized stepwise process of protein gathering, lipid accumulation, and recognition by Plin2 and Plin3. The concentration of arriving lipids determines the rate of growth of emerging LDs but not the copy number of emerging structures, which suggests that the nucleation domains are predefined in the ER. Third, after this initial nucleation, and proportionally to lipid availability, more LDs will be progressively nucleated. Restricted by a relatively constant maximal size of individual LDs, cells nucleate additional LDs to store additional lipids (Fig. 7, G and H).

We hypothesize that these successive events reflect different stages of the same stepwise maturation process (Fig. 10). This scenario is possible because emerging LDs are stable in the absence of an additional lipid supply. Lipid arrival will promote gradual progression of each step into the next, but lipid depletion will stop progression, though not reverse it, until new lipid arrives. A possible explanation for such stability is that these early LDs may not have acquired the protein composition that facilitates lipolysis, and thus, maturation of LDs may be necessary to allow access of lipases. The existence of a set of LDs resistant to starvation guarantees efficient packaging in the ER of occasional lipids, and if lipid arrival persists, the assembly of new LDs will allow medium- and long-term storage. Further, because LDs are not simply sites of lipid storage but are also involved in other cellular functions, such as protein

storage (Welte, 2007), protein degradation (Wang and Lee, 2012), or immunity (Anand et al., 2012), the stability of the pre-LDs might facilitate these roles even during a prolonged absence of extracellular lipids.

How and where are these pre-LDs and LDs formed? Most models suggest that LDs originate in the ER bilayer and then remain connected to the ER, or alternatively bud off to become independent organelles (Walther and Farese, 2012). Based on freeze-fracture electron microscopy, it has been proposed that the LDs grow within a concave depression of the ER or “egg-cup” (Robenek et al., 2006). Other models hypothesize vesicular budding (Walther and Farese, 2009) or bicelle excision from the ER (Ploegh, 2007).

Here, our simultaneous visualization of emerging LDs (HPos) and the neighboring ER tubules (HNeu), in conjunction with the electron tomography, supports the overall hypothesis that LDs do indeed originate in the ER. HPos rapidly moves from the ER into pre- and nascent LDs and, at least during the initial steps of biogenesis, all our images demonstrate that LDs are in contact with the ER (Figs. 2, 5, 8, and S1). Electron microscopy and tomography confirm that LDs are clearly surrounded by a single monolayer, which is consistent with the idea that neutral lipid deposition occurs between the two leaflets of the ER bilayer. Rather than an “eggcup,” the tomography demonstrates multiple but discrete interactions between the ER and LDs and in some cases a likely continuity between both membranes. Real-time microscopy of emerging LD formation did not show perceptible budding or detachment processes

involving ER membranes (Fig. 3). Further, bicelle formation or vesicular budding are inconsistent with the observation that LDs often have extended connections with neighboring LDs.

Thus, we favor a “blister-like” organization of lipid globules in the bilayer, observed in early electron microscopy studies of the ER of plants and proposed using simulation models (Wanner et al., 1981; Khandelia et al., 2010). Initially, newly synthesized neutral lipids can be integrated in the ER membrane (for review see Suzuki et al., 2011). However, continuous lipid arrival increases the relative concentration of triacylglycerols in the membrane, promoting phase separation, and the deposition of globules of neutral lipids between the two leaflets of the ER bilayer. Biophysical models predict that the diameters of these primordial globules are ~ 20 nm (Zanghellini et al., 2010). These globules can already cause transient curvature of the ER membrane, or move two-dimensionally within the bilayer, fusing with other globules, and generate a more pronounced curvature (Khandelia et al., 2010; Suzuki et al., 2011; Fig. 10). Proteins with amphipathic α helices anchored to the cytosolic side of the ER can rapidly recognize curved membranes, acting as neutral lipid sensors (McMahon and Gallop, 2005). Consistent with this hypothesis, a significant number of proteins are anchored to LDs by amphipathic helices (for review see Walther and Farese, 2012). The strong and stable interaction of these proteins with the membrane likely provides the equilibrium required to nucleate unstable globules in defined ER sites, mark the onset of LD biogenesis, and produce the blister-like morphology of the ER bilayer.

The above mechanism could accumulate ACSL3 at these ER sites, as this enzyme contains amphipathic helices (Poppelreuther et al., 2012). Our preliminary *in silico* analysis confirms this possibility for ACSL3 and HPos (Fig. S5). In any case, enrichment of ACSL3 on emerging LDs will generate a concomitant local enrichment of acyl-CoA, which is essential to synthesize lysophosphatidic acid, diacylglycerol, triacylglycerol, and phospholipids required to increase the size of the primordial globule and the expansion of the emerging LD (Kuerschner et al., 2008; Skinner et al., 2009; Adeyo et al., 2011; Fei et al., 2011; Kraemer et al., 2011; Moessinger et al., 2011; Wilfling et al., 2013). In parallel, transient generation of active lipid intermediates, such as phosphatidic acid and diacylglycerol, will also modify the shape of the membrane and recruit proteins (for review see Brasaemle and Wolins, 2012). Such a self-reinforcing process is consistent with the kinetics of delayed formation of emerging LDs after lipid arrival and with the observation that pre-LDs, containing ACSL3, are able to initially pack arriving lipids more rapidly.

The ACSL family mediates the conversion of long-chain fatty acids into acyl-CoA, and it is assumed that each ACSL isoform channels with high specificity the fatty acid to distinct metabolic fates (Ellis et al., 2010). Although the presence of ACSL1 and ACSL4 on LDs was suggested by proteomic analysis (Brasaemle et al., 2004; Liu et al., 2004; Wilfling et al., 2013), this finding was questioned (Poppelreuther et al., 2012). In contrast, it seems accepted that the ACSL3 is on LDs, and accordingly a role of this enzyme during LD biogenesis was proposed. Here, we have experimentally addressed this possibility and

demonstrated that ACSL3 channels fatty acids into nascent LDs. The absence of ACSL3 significantly reduces nucleation of emerging LDs, short- and long-term accumulation of neutral lipids, and the size and number of mature LDs. On the contrary, down-regulation or overexpression of other family members did not modify the process. Reduced ACSL3 levels in the nucleation sites likely decrease local accumulation of acyl-CoA, decrease substrate availability for the reactions described above, and thus reduce the efficiency of the process that relies on lipids activated elsewhere. Interestingly, similarly to perilipins, the expression of the ACSL family members is regulated during differentiation of 3T3 fibroblasts into adipocytes. ACSL1 is up-regulated (similar to Plin1) but ACSL3 is highly down-regulated (similar to Plin2 and Plin3; Sandoval et al., 2008). Thus, in mature 3T3 adipocytes it is likely that factors other than ACSL3 assist LD nucleation and expansion.

Although the enzymatic activity of ACSL3 is crucial for LD formation, clearly suggested by the complete inhibition caused by Triacsin C, other functions might also be important, as ACSL3 lacking enzymatic activity also increased LD nucleation. Although this initial observation requires further analysis, and ACSL3's amphipathic helices might simply contribute to membrane curvature as suggested above, the capacity of ACSL3 for interaction with other LD proteins could potentially organize specific regions within the complex mixture of proteins and lipids residing in or in transit on the ER tubules. Indeed, ACSL3 interacts with Spartin/SPG20 and AUP1 that are in turn crucial scaffolding proteins that determine LD composition, size, and numbers (Milewska et al., 2009; Klemm et al., 2011). Accordingly, ACSL3 has been found in complexes with neutral lipid synthesis enzymes (Wilfling et al., 2013). In addition, dynamic relocation of the enzyme between the ER tubules, pre-LDs, and LDs might represent a cellular homeostatic sensor given that ACSL3 regulates the activity of key lipogenic transcription factors such as PPAR- γ , ChREBP, SREBP1-c, and LXR- α (Bu et al., 2009).

In conclusion, the model proteins generated for this study enabled us to anticipate, visualize, and characterize LDs emerging from the ER membranes. We demonstrate that early LDs are stable ER microdomains in the absence of lipid supply, and that lipid storage occurs via multiple processes with different kinetics. Finally, we have shown that ACSL3 is important for efficient LD nucleation and that ACSL3 is the family member that efficiently channels lipids into nascent LDs.

Materials and methods

Antibodies and reagents

OA and mowiol were obtained from EMD Millipore. Fatty acid-free BSA (A8806), palmitic acid, sucrose, saponin, brefeldin A, platanisimycin, cycloheximide, and Nile red were obtained from Sigma-Aldrich. BODIPY 493/503, Hoechst-33258, and BODIPY-FL C16 were from Molecular Probes. LipidTOX Deep Red Neutral Lipid Stain was from Life Technologies, Invitrogen. Paraformaldehyde was from Electron Microscopy Sciences and Triacsin C from Santa Cruz Biotechnology, Inc.

Rabbit polyclonal antibody anti-GFP (ab290), rabbit polyclonal anti-Plin2 (ab52355), rabbit polyclonal anti-ACSL1 (ab76702), rabbit monoclonal anti-ACSL4/FACL4 (ab155282), mouse monoclonal anti-actin (ab40864), and mouse monoclonal anti-c-myc (ab32) were from Abcam. Rabbit polyclonal anti-Sec61 α (07-204) was from EMD Millipore. The

mouse polyclonal anti-ACSL3 (B01P) was from Abnova. Guinea pig polyclonal antibody against Plin3 was from Progen. Alexa Fluor 555- and 647-conjugated secondary antibodies were from Life Technologies, Invitrogen.

Silencer siRNAs against human ACSL1, ACSL3, and ACSL4 were obtained from QIAGEN in a FlexiTube format. The siRNA target sequences were as follows: For ACSL1, 5'-AAGGATGCTTGTATTTCGA-3', 5'-TCG-CAGCGGCATCATCAGAAA-3', 5'-CAGGTGTTGTCCACGGAGAAA-3'; for ACSL3, 5'-CCGAAGTGTGGGACTACAATA-3', 5'-AACCACGCAGC-GATTCATGAA-3', 5'-ACCGCGTGAGTTAAGATTTAA-3', and 5'-TAGCT-GAAAGAAAGGACTTA-3'; for ACSL4, 5'-ATGCATCATAGCAATTTGATA-3', 5'-TTGGAGCGATTGAAAATCCA-3', 5'-CAGATTATAGATCGTAAGAAA-3', and 5'-AAGGGCAGAGTACTTGATAA-3'. The nonrelated siRNA used was against GFP from Thermo Fisher Scientific.

Plasmids

Mutant proteins were N-terminally tagged with the GFP (unless otherwise indicated). Standard YUX cloning, using primers containing BspEI (forward) and SmaI (backward) restriction sites, was used to synthesize GFP-HPos and GFP-HNeu. The orange-tagged HPos mutant was obtained after subcloning of the GFP-HPos into mOrange expression vector provided by R.Y. Tsien (Howard Hughes Medical Institute, Chevy Chase, MD). The mOrange expression vector was obtained by amplification of the fluorescent protein with a 5' primer encoding an AgeI site and a 3' primer encoding a BspEI site and ligated into similarly digested pEGFP-C1 (Takara Bio Inc.) cloning vector backbones. The pEGFP-DGAT2 construct was derived from the plasmid pCDNA3-Flag-DGAT2 provided by R.V. Farese (Gladstone Institute of Cardiovascular Disease, San Francisco, CA) and subcloned into a pEGFP-C3 expression vector to generate a GFP fusion. The pCDNA4/TO-myc-ACSL3 was provided by N. Yamaguchi (Graduate School of Pharmaceutical Sciences, Chiba, Japan). The construct was generated by subcloning human myc-ACSL3 cDNA into pCDNA4/TO vector (Invitrogen). pCDNA 3xmyc-tagged Plin3 was provided by S. Pfeffer (Stanford University School of Medicine, Stanford, CA). The construct was obtained by amplification of the full length by PCR with the introduction of EcoRI and XbaI sites for cloning into pCDNA3.1 and a 5' EcoRV site for the insertion of the 3x Myc repeats generated by PCR. The pEFGP vector encoding human Plin2 was provided by J. McLauchlan (Institute of Virology, Glasgow, Scotland).

For the expression vector encoding siRNA-resistant ACSL3, five silent mutations were introduced in each of the four siRNA target sequences. The construct ACSL3 Δ Gate results from deletion of the amino acids 314–339 (fatty acid Gate domain; Soupene et al., 2010) from siRNA-resistant ACSL3. Both cDNAs were purchased from GenScript and subcloned in pEGFP vector. GFP-tagged expression vectors containing human cDNAs for ACSL1, ACSL4, and ACSL5 (catalog Nos. RG208196, RG205356, RG201076, respectively) were purchased from OriGene.

Cell culture

COS-1 cells (African green monkey kidney fibroblast-like cell line) were cultured in 5% vol/vol FCS and Huh7 and HepG2 (human hepatoma cell lines) in 10% vol/vol FCS (Biological Industries). All cells were maintained at 37°C and 5% CO₂ in DMEM (Biological Industries) supplemented with 4 mM L-glutamine (Sigma-Aldrich), 1 mM pyruvate (Sigma-Aldrich), nonessential amino acids (Biological Industries), 50 U/ml penicillin, and 50 μ g/ml streptomycin sulfate (Biological Industries). Starvation was performed by culturing cells in DMEM, L-glutamine, pyruvate, and nonessential amino acids but in the absence of serum for 24 h. To promote the formation of LDs, cells were treated with OA and/or palmitic acid conjugated to fatty acid-free BSA at a molar ratio of 6:1 and added to the culture medium to give a final concentration of 175 μ g/ml (unless other concentration is specified).

Transfections

The siRNA transfections were performed using Lipofectamine RNAiMAX reagent (Invitrogen, Life Technologies). All procedures were performed according to the manufacturer's instructions. For DNA transfection experiments, cells plated at 18,000 cells/cm² on glass coverslips the day before were transfected with the corresponding fusion proteins using Effectene Transfection Reagent (QIAGEN). To reduce the number of LDs, transfection was performed in DMEM supplemented with 0.5% FCS and changed to DMEM without serum 6 h after transfection. The precise concentration of each construct was specifically adjusted to get a similar expression and transfection efficiency. In experiments involving siRNA and DNA transfections, the DNA was transfected 24 h later than the siRNA.

Confocal microscopy

Cells were fixed in 4% PFA diluted in PBS for 1 h at room temperature. In some experiments, fixed cells were stained with Nile red added to Mowiol at 1:1,000 dilution (from saturated stock solution in acetone) or BODIPY 493/503 for 30 min in PBS. For immunofluorescence microscopy, fixed cells were permeabilized in 0.1% saponin in PBS for 10 min at RT, and blocked with 0.2% BSA in PBS for 10 min at room temperature. Then cells were incubated with anti-ACSL3 (1:200), anti-Plin2/ADRP (1:100), anti-Plin3/TIP47 (1:200) or anti-myc (1:250) for 1 h at room temperature, followed by three washes in PBS and incubation with Alexa Fluor 555- or 647-conjugated anti-mouse or anti-rabbit IgG antibody (1:250) for 45 min, washed in PBS, and mounted in Mowiol (Sigma-Aldrich).

Cells were examined using a 63x oil immersion objective in a laser scanning confocal microscope (TCS SL; Leica) with a pinhole of 1.5 AU. All images are single confocal sections. For quantification, transfected cells were randomly selected, and image analysis was performed with Photoshop CS software (Adobe). The quantifications of size and number of pre-LDs and emerging LDs, and the colocalization of transfected proteins with HPos, were performed in three independent experiments and at least 20 cells per experiment using ImageJ software (National Institutes of Health).

The number and size of mature LDs (Fig. 7, G and H) was calculated using the custom-written MATLAB code. In these experiments, living cells were labeled by addition of 0.3 μ M Hoechst-33258 and 0.83 μ g/ml Nile red in the culture media. Cells were randomly selected, and images were captured in a laser scanning confocal spectral microscope (TCS SP5; Leica) equipped with an incubation control system (37°C and 5% CO₂) with a 63x oil immersion objective lens with an NA of 1.4, using a 405-nm and 561-nm laser lines, respectively. Mean area of a single LD was calculated by scoring all the structures that were <800 nm in diameter, which is the diameter of the largest single LD observed. Images were acquired with a pixel size of 80 nm to accurately resolve these structures, according to Nyquist theorem. The sum total of the areas of all LDs whose diameter was <800 nm was divided by the number of LDs <800 nm in diameter. Cells treated with high OA had clusters with inseparable LDs. To estimate the number of LDs/cell in such cells, the total area of LDs including the clusters was divided by the mean area of single LD in each cell.

Time-lapse video microscopy

Time-lapse video microscopy was performed with a laser scanning confocal spectral microscope (TCS SP5; Leica) equipped with an incubation control system (37°C, 5% CO₂). Cells were transfected and treated as explained above. In some experiments, cells were additionally treated with 10 μ g/ml of cycloheximide for 3 h to reduce the pool of newly synthesized protein. Cells were selected for the labeling of well-defined ER elements. OA (175 μ g/ml) and in some cases BODIPY-FLC16 (FA-BODIPY, 1 μ M) were added and images were captured every 9 s with a 63x oil immersion objective lens with an NA of 1.4, at 6x zoom, using 488-nm and 561-nm laser lines. Movies were digitally treated with the Leica Application Suite software (3.10 build 8587). In the experiments using FA-BODIPY, the mean background fluorescence was calculated from at least three different cytosolic regions at time 0 (just before the addition of the green fatty acid). This background was identically subtracted from all the frames of the movies. In the case of the transfected peptides, the mean unspecific background was calculated from an extracellular region at time 0 and identically subtracted from all the frames of the movies. Finally, all the frames of the movies were identically filtered with a Gaussian blur filter using radius 2. Fluorescence intensity and LDs size were quantified using Photoshop CS software (Adobe) from three independent experiments and at least 20 structures per experiment.

FRAP

FRAP experiments were performed on a laser scanning confocal spectral microscope (TCS SP5; Leica) equipped with an incubation control system (37°C, 5% CO₂). A defined region of interest (ROI, 0.5 μ m of diameter) was photobleached at full laser power (100% power, 50–80 iterations), and recovery of fluorescence was monitored by scanning the ROI at low laser power (1–4% of laser power, 20 s of 0.75-s interval scans). Fluorescence intensity was normalized to the prebleach intensity. Any loss of fluorescence during the recording was corrected with unbleached regions of the cell. The values were fitted to a nonlinear regression equation, $F(t) = M[1 - \exp(-t/t_{1/2})]$, where F is the fluorescence intensity, M is the mobile fraction, and $t_{1/2}$ is the time constant.

Electron microscopy and tilting tomography

COS-1 cells cultured on carbon-coated sapphire discs were starved, treated with OA, and further incubated as described above. Cells were then fast-frozen, freeze-substituted, and embedded in HM20 resin at low temperature (Nixon et al., 2009). 300-nm sections, nonspecifically labeled with gold as fiducial markers, were imaged using an intermediate voltage EM (Tecnaï F30; FEI Company) operated at 300 kV, and motorized tilt-rotate specimen holders (models 650 and CT3500TR; Gatan, Inc.). Tilt series images (each 2,048 × 2,048 pixels) were digitally acquired with an Ultra-Scan 4000 (USC4000, model 895; Gatan, Inc.). Dual-axis tilt series, collected over a total angular tilt range from -62° to $+62^\circ$ at 1° increments, were first aligned with one another by cross-correlation and subsequently by precisely tracking the positions of gold fiducials using the tiltalign program that is part of the imod software package (versions used: 3.10.5–3.11.1; Richter et al., 2008).

Isolation of LDs

Two 10-cm dishes of COS-1 cells were transfected and treated as described above. Cells were washed twice with cold PBS and resuspended in 500 μ l of homogenization buffer (50 mmol/liter Tris-HCl, pH 7.5, 150 mmol/liter sodium chloride, and 5 mmol/liter EDTA), supplemented with 10 μ g/ml leupeptin and 10 μ g/ml aprotinin. Cells were disrupted at 4°C by nitrogen cavitation in a cell disruption bomb (ref. 46.39; Parr Instrument Company) at 800 psi for 15 min and collected dropwise. Afterward, cells were passed back and forth through a 22-gauge needle 25 times at 4°C . Nuclei and unbroken cells were removed by centrifugation at 1,600 *g* in a MLA-130 rotor (Beckman Coulter) for 5 min at 4°C . The resulting supernatant (500 μ l) was mixed with an equal volume of 2.5 M sucrose and loaded at the bottom of a discontinuous sucrose gradient formed by layers of 200 μ l of 30, 25, 20, 15, 10, and 5% sucrose (wt/vol) freshly prepared in homogenization buffer. Gradients were centrifuged in a TLS-55 swinging-rotor (Beckman Coulter) without brake at 166,000 *g* for 3 h at 4°C . Five fractions of 280 μ l were collected from the top in addition to a final lower fraction of 700 μ l by using a CentriTube Slicer (Beckman Coulter). The gradients shown in the figures are representative of at least two independent experiments.

Flow cytometry analysis

To determine neutral lipid accumulation after treatments, cells were trypsinized, washed in PBS, and stained with Nile red (Gubern et al., 2008). Samples were analyzed by flow cytometry in a FACS Cantoll equipped with a 488-nm argon laser and a 635-nm red diode laser (BD). Yellow emission of Nile red, corresponding to the neutral lipid staining, was measured in the 585/42 filter set. To determine neutral lipid content in GFP-transfected cells, after the treatments, cells were trypsinized, washed in PBS, and fixed in 4% PFA for 30 min. Cells were stained with LipidTOX Deep Red Neutral Lipid Stain (1:10,000; Life Technologies) and analyzed by flow cytometry. Deep Red emission of LipidTOX was measured in the 660/20 filter set. For the staining of cells transfected with myc-ACSL3, cells were trypsinized, washed in PBS, and fixed in 4% PFA for 1 h, followed by saponin permeabilization (0.1% in PBS) for 10 min. After a 10-min incubation in 0.2% BSA, cells were labeled with anti-myc antibody (1:250) for 1 h at room temperature in blocking solution, followed by incubation with secondary antibody goat anti-mouse Alexa Fluor 647. To analyze neutral lipid content, these cells were stained with BODIPY 493/503 (Bulankina et al., 2009) and analyzed by flow cytometry; green emission of BODIPY 493/503 was measured in the 530/30 filter set and far red emission of Alexa Fluor 647 in the 660/20 filter set. The use of BODIPY 493/503 in the case of transfected cells was to avoid the interference of the Nile red emission with the far-red emission of the secondary antibody, as Nile red also has red fluorescence when it is solvated in a phospholipid-rich environment (Greenspan et al., 1985).

Fluorescent thin layer chromatography

Cells treated with OA and BODIPY-FLC16 for the indicated times were trypsinized and resuspended in 600 μ l of methanol/chloroform (1:2), then 250 μ l of chloroform and 250 μ l of water were added and the solution was mixed by vortex (Bligh and Dyer, 1959). After a spin, the organic phase was collected, dried, resuspended with chloroform, and spotted onto 60 \AA silica gel TLC plates (Partisil LK6D; Whatman) and dried for several minutes. A solvent system of hexane/diethyl ether/acetic acid (70:30:1) was added to the TLC chamber and allowed to equilibrate, and plates were run until the solvent front reached 1 cm from the top of the plate. After drying, plates were scanned (ImageQuant LAS4000 biomolecular imager; GE Healthcare) using the blue fluorescence light (excitation, 460 nm; emission, Y515Di filter) to detect fluorescent bands.

Western blotting

Gel electrophoresis and Western blotting were performed as described previously (Turró et al., 2006). Membranes were incubated with anti-GFP (1:1,000), anti-ACSL1 (1:500), anti-ACSL3 (1:1,000), anti-ACSL4/FACL4 (1:10,000), anti-actin (1:10,000), anti-sec61 (1:1,000), or anti-Plin2 (1:500). After the incubation with primary antibody (see antibodies section for details of the antibodies), the membrane was washed and incubated with peroxidase-conjugated secondary antibodies (1:3,000 dilution; Bio-Rad Laboratories), and detected using ECL detection (Biological Industries, Ltd.) on medical x-ray film (Fujifilm).

Acyl-CoA synthase activity

Total acyl-CoA synthetase activity was measured as described previously (Asp et al., 2009). In brief, cells were harvested in 200 μ l of ACSL buffer (50 mM KH_2PO_4 , 10% glycerol, and 1 mM EDTA, pH 7.4) at 4°C and lysed by sonication. Protein was quantified and 100 μ g of protein was incubated during 20 min at 37°C in a reaction mix containing 175 mM Tris-HCl, 8 mM MgCl_2 , 5 mM dithiothreitol, 10 mM ATP, 250 μ M coenzyme A sodium salt (C3144; Sigma-Aldrich), and 50 μ M (0.2 μ Ci) of BSA-conjugated OA trace-labeled with [$1\text{-}^{14}\text{C}$]OA (NEC-317; PerkinElmer) at 1:6 mol/mol. After that, 1 ml of Doles reagent (2-propanol/hexane/ H_2SO_4 at 8:2:0.2), 2 ml of heptane, and 0.5 ml of water were added to each tube, and, after a vortex, the organic phase was discarded. Then, the aqueous phase was washed three times, adding 2 ml of heptane, and, after a vortex, the organic phase was discarded. Finally, the radioactivity of the aqueous phase was read.

Real-time PCR

Total RNA was isolated from cells using the RNeasy Mini kit (QIAGEN) according to the manufacturer's instructions. 1 μ g of total RNA was used for cDNA synthesis, using the High Capacity cDNA Reverse Transcription kit (Applied Bioscience; Life Technologies) according to the manufacturer's instructions. qRT-PCR was performed using the Brilliant SYBR Green qPCR Master Mix (600548; Agilent Technologies) and detected by the Mx3000P System (Agilent Technologies). The relative expression of each mRNA normalized to the internal reference RPL13 was analyzed using the $2^{-\Delta\Delta\text{C}}$ method (Butler and Mallampalli, 2010).

The primers used for real-time PCR were: ACSL1 forward, 5'-GGG-AAGAGCCAAACAGACGGAAGC-3', and reverse, 5'-CATATGGGCGAGAGGCAAGAAAGA-3'. ACSL3 forward, 5'-GGGACTTGGGAGGAGCTGTGTAAC-3', and reverse 5'-CTCAATGTCCGCTGGTAATGTGT-3'. ACSL4 forward, 5'-GGGGCCCCGCTATCTCCTC-3', and reverse 5'-CCTCTGGGTTTGGCTTGTAT-3'. RPL13 forward, 5'-ATGGCGGAGGGGCGAGTTCT-3', and reverse 5'-CTCGGGAGGGGTTGGTATTCA-3'.

In silico analysis of α helix formation

The in silico analysis of putative amphipathic helices in the amino acid sequence of HPOs and human ACSL3 were predicted by the HELIQUEST program (<http://heliquest.ipmc.cnrs.fr/>) according to the method previously published in Gautier et al. (2008).

Statistical analysis

All graphs correspond to the mean and standard deviation of at least three independent experiments. Statistical significances were determined using the Student's *t* test; *, $P < 0.05$; **, $P < 0.01$; ***, $P < 0.001$.

Online supplemental material

Fig. S1 (related to Fig. 5) includes a detailed colocalization between HPOs and ACSL3, Plin 2, or Plin3. Fig. S2 (related to Fig. 7) compares the role of ACSL3 with ACSL1, ACSL4, and ACSL5 during LD assembly and neutral lipid accumulation. Fig. S3 (related to Fig. 7) demonstrates that the expression of an siRNA-resistant form of ACSL3 recovers the assembly and accumulation of LDs inhibited after the siRNA of ACSL3. Fig. S4 (related to Fig. 7) shows that ACSL3 also regulates LD assembly and neutral lipid accumulation in hepatic cell lines. Fig. S5 (related to the Discussion) shows putative amphipathic α helices of HPOs and ACSL3. Video 1 is related to Fig. 3 A and shows the biogenesis of LDs in the membranes of the ER. Videos 2 and 3 are related to Fig. 2 A and shows how pre-LDs and emerging LDs are loaded with a fluorescent fatty acid. Videos 4 and 5 show the tilting tomography of LDs detailed in Fig. 9. Also included is the code used to determine the number and size of mature LDs performed in Fig. 7 (Code areaMultipleImages-2.txt and instructions.doc). Online supplemental material is available at <http://www.jcb.org/cgi/content/full/jcb.201305142/DC1>.

We thank Dr. Maria Calvo and Anna Bosch for help with confocal microscopy (Serveis Científico-Tècnics de la Universitat de Barcelona) and Maria Molinos for technical assistance.

A. Pol is supported by grants BFU2011-23745 and CSD2009-00016 (from Ministerio de Economía y Competitividad [MICINN] and Marató de TV3), and R.G. Parton was supported by a fellowship from the National Health and Medical Research Council of Australia (grant No. 569542). F. Tebar was supported by BFU2009-13526 (MICINN), C. Enrich by BFU2009-10335 (MICINN), CSD2009-00016 (MICINN and Marató de TV3), and S.P. Gross by GM64624 (National Institutes of Health). The authors acknowledge the facilities, and the scientific and technical assistance, of the Australian Microscopy and Microanalysis Research Facility at the Centre for Microscopy and Microanalysis, the University of Queensland. We are indebted to the Citomics unit of the Institut d'Investigacions Biomèdiques August Pi i Sunyer and the Centre for Microscopy and Microanalysis at the University of Queensland for their technical help.

Submitted: 28 May 2013

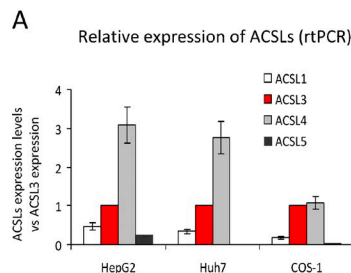
Accepted: 10 November 2013

References

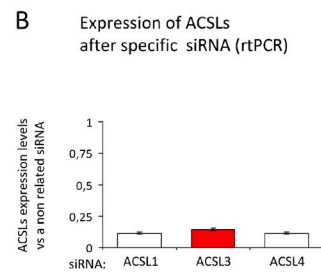
- Adeyo, O., P.J. Horn, S. Lee, D.D. Binns, A. Chandras, K.D. Chapman, and J.M. Goodman. 2011. The yeast lipin orthologue Pah1p is important for biogenesis of lipid droplets. *J. Cell Biol.* 192:1043–1055. <http://dx.doi.org/10.1083/jcb.201010111>
- Anand, P., S. Cermelli, Z. Li, A. Kassan, M. Bosch, R. Sigua, L. Huang, A.J. Ouellette, A. Pol, M.A. Welte, and S.P. Gross. 2012. A novel role for lipid droplets in the organismal antibacterial response. *Elife*. 1:e00003. <http://dx.doi.org/10.7554/eLife.00003>
- Asp, L., F. Kartberg, J. Fernandez-Rodriguez, M. Smedh, M. Elsnér, F. Laporte, M. Bárcena, K.A. Jansen, J.A. Valentijn, A.J. Koster, et al. 2009. Early stages of Golgi vesicle and tubule formation require diacylglycerol. *Mol. Biol. Cell.* 20:780–790. <http://dx.doi.org/10.1091/mbc.E08-03-0256>
- Bligh, E.G., and W.J. Dyer. 1959. A rapid method of total lipid extraction and purification. *Can. J. Biochem. Physiol.* 37:911–917. <http://dx.doi.org/10.1139/o59-099>
- Bosch, M., M. Marí, S.P. Gross, J.C. Fernández-Checa, and A. Pol. 2011. Mitochondrial cholesterol: a connection between caveolin, metabolism, and disease. *Traffic*. 12:1483–1489. <http://dx.doi.org/10.1111/j.1600-0854.2011.01259.x>
- Braasemle, D.L., and N.E. Wolins. 2012. Packaging of fat: an evolving model of lipid droplet assembly and expansion. *J. Biol. Chem.* 287:2273–2279. <http://dx.doi.org/10.1074/jbc.R111.309088>
- Braasemle, D.L., B. Rubin, I.A. Harten, J. Gruja-Gray, A.R. Kimmel, and C. Londos. 2000. Perilipin A increases triacylglycerol storage by decreasing the rate of triacylglycerol hydrolysis. *J. Biol. Chem.* 275:38486–38493. <http://dx.doi.org/10.1074/jbc.M007322200>
- Braasemle, D.L., G. Dolios, L. Shapiro, and R. Wang. 2004. Proteomic analysis of proteins associated with lipid droplets of basal and lipolytically stimulated 3T3-L1 adipocytes. *J. Biol. Chem.* 279:46835–46842. <http://dx.doi.org/10.1074/jbc.M409340200>
- Bu, S.Y., M.T. Mashek, and D.G. Mashek. 2009. Suppression of long chain acyl-CoA synthetase 3 decreases hepatic de novo fatty acid synthesis through decreased transcriptional activity. *J. Biol. Chem.* 284:30474–30483. <http://dx.doi.org/10.1074/jbc.M109.036665>
- Buhman, K.K., H.C. Chen, and R.V. Farese Jr. 2001. The enzymes of neutral lipid synthesis. *J. Biol. Chem.* 276:40369–40372. <http://dx.doi.org/10.1074/jbc.R100050200>
- Bulankina, A.V., A. Deggerich, D. Wenzel, K. Mutenda, J.G. Wittmann, M.G. Rudolph, K.N. Burger, and S. Höning. 2009. TIP47 functions in the biogenesis of lipid droplets. *J. Cell Biol.* 185:641–655. <http://dx.doi.org/10.1083/jcb.200812042>
- Butler, P.L., and R.K. Mallampalli. 2010. Cross-talk between remodeling and de novo pathways maintains phospholipid balance through ubiquitination. *J. Biol. Chem.* 285:6246–6258. <http://dx.doi.org/10.1074/jbc.M109.017350>
- Carten, J.D., M.K. Bradford, and S.A. Farber. 2011. Visualizing digestive organ morphology and function using differential fatty acid metabolism in live zebrafish. *Dev. Biol.* 360:276–285. <http://dx.doi.org/10.1016/j.ydbio.2011.09.010>
- Ellis, J.M., J.L. Frahm, L.O. Li, and R.A. Coleman. 2010. Acyl-coenzyme A synthetases in metabolic control. *Curr. Opin. Lipidol.* 21:212–217. <http://dx.doi.org/10.1097/MOL.0b013e32833884bb>
- Fei, W., G. Shui, Y. Zhang, N. Krahrmer, C. Ferguson, T.S. Kapterian, R.C. Lin, I.W. Dawes, A.J. Brown, P. Li, et al. 2011. A role for phosphatidic acid in the formation of “supersized” lipid droplets. *PLoS Genet.* 7:e1002201. <http://dx.doi.org/10.1371/journal.pgen.1002201>
- Fernández-Rojo, M.A., C. Restall, C. Ferguson, N. Martel, S. Martin, M. Bosch, A. Kassan, G.M. Leong, S.D. Martin, S.L. McGee, et al. 2012. Caveolin-1 orchestrates the balance between glucose and lipid-dependent energy metabolism: implications for liver regeneration. *Hepatology*. 55:1574–1584. <http://dx.doi.org/10.1002/hep.24810>
- Fujimoto, Y., H. Itabe, J. Sakai, M. Makita, J. Noda, M. Mori, Y. Higashi, S. Kojima, and T. Takano. 2004. Identification of major proteins in the lipid droplet-enriched fraction isolated from the human hepatocyte cell line HuH7. *Biochim. Biophys. Acta*. 1644:47–59. <http://dx.doi.org/10.1016/j.bbamcr.2003.10.018>
- Fujimoto, Y., H. Itabe, T. Kinoshita, K.J. Homma, J. Onoduka, M. Mori, S. Yamaguchi, M. Makita, Y. Higashi, A. Yamashita, and T. Takano. 2007. Involvement of ACSL in local synthesis of neutral lipids in cytoplasmic lipid droplets in human hepatocyte HuH7. *J. Lipid Res.* 48:1280–1292. <http://dx.doi.org/10.1194/jlr.M700050-JLR200>
- Gautier, R., D. Douguet, B. Antonny, and G. Drin. 2008. HELIQUEST: a web server to screen sequences with specific alpha-helical properties. *Bioinformatics*. 24:2101–2102. <http://dx.doi.org/10.1093/bioinformatics/btn392>
- Greenspan, P., E.P. Mayer, and S.D. Fowler. 1985. Nile red: a selective fluorescent stain for intracellular lipid droplets. *J. Cell Biol.* 100:965–973. <http://dx.doi.org/10.1083/jcb.100.3.965>
- Gubern, A., J. Casas, M. Barceló-Torns, D. Barneda, X. de la Rosa, R. Masgrau, F. Picatoste, J. Balsinde, M.A. Balboa, and E. Claro. 2008. Group IVA phospholipase A2 is necessary for the biogenesis of lipid droplets. *J. Biol. Chem.* 283:27369–27382. <http://dx.doi.org/10.1074/jbc.M800696200>
- Hermes, A., M. Bosch, N. Ariotti, B.J. Reddy, A. Fajardo, A. Fernández-Vidal, A. Alvarez-Guaita, M.A. Fernández-Rojo, C. Rentero, F. Tebar, et al. 2013. Cell-to-cell heterogeneity in lipid droplets suggests a mechanism to reduce lipotoxicity. *Curr. Biol.* 23:1489–1496. <http://dx.doi.org/10.1016/j.cub.2013.06.032>
- Ingelmo-Torres, M., E. González-Moreno, A. Kassan, M. Hanzal-Bayer, F. Tebar, A. Herms, T. Grewal, J.F. Hancock, C. Enrich, M. Bosch, et al. 2009. Hydrophobic and basic domains target proteins to lipid droplets. *Traffic*. 10:1785–1801. <http://dx.doi.org/10.1111/j.1600-0854.2009.00994.x>
- Jacquier, N., V. Choudhary, M. Mari, A. Toulmay, F. Reggiori, and R. Schneider. 2011. Lipid droplets are functionally connected to the endoplasmic reticulum in *Saccharomyces cerevisiae*. *J. Cell Sci.* 124:2424–2437. <http://dx.doi.org/10.1242/jcs.076836>
- Khandelia, H., L. Duellund, K.I. Pakkanen, and J.H. Ipsen. 2010. Triglyceride blisters in lipid bilayers: implications for lipid droplet biogenesis and the mobile lipid signal in cancer cell membranes. *PLoS ONE*. 5:e12811. <http://dx.doi.org/10.1371/journal.pone.0012811>
- Klemm, E.J., E. Spooner, and H.L. Ploegh. 2011. Dual role of ancient ubiquitous protein 1 (AUP1) in lipid droplet accumulation and endoplasmic reticulum (ER) protein quality control. *J. Biol. Chem.* 286:37602–37614. <http://dx.doi.org/10.1074/jbc.M111.284794>
- Krahrmer, N., Y. Guo, F. Wilfling, M. Hilger, S. Lingrell, K. Heger, H.W. Newman, M. Schmidt-Supprian, D.E. Vance, M. Mann, et al. 2011. Phosphatidylcholine synthesis for lipid droplet expansion is mediated by localized activation of CTP:phosphocholine cytidylyltransferase. *Cell Metab.* 14:504–515. <http://dx.doi.org/10.1016/j.cmet.2011.07.013>
- Kuerschner, L., C. Moessinger, and C. Thiele. 2008. Imaging of lipid biosynthesis: how a neutral lipid enters lipid droplets. *Traffic*. 9:338–352. <http://dx.doi.org/10.1111/j.1600-0854.2007.00689.x>
- Lacey, D., F. Beaudoin, C.E. Dempsey, P.R. Shewry, and J.A. Napier. 1999. The accumulation of triacylglycerols within the endoplasmic reticulum of developing seeds of *Helianthus annuus*. *Plant J.* 17:397–405. <http://dx.doi.org/10.1046/j.1365-313X.1999.00387.x>
- Le Lay, S., E. Hajdúch, M.R. Lindsay, X. Le Lièvre, C. Thiele, P. Ferré, R.G. Parton, T. Kurzchalia, K. Simons, and I. Dugail. 2006. Cholesterol-induced caveolin targeting to lipid droplets in adipocytes: a role for caveolar endocytosis. *Traffic*. 7:549–561. <http://dx.doi.org/10.1111/j.1600-0854.2006.00406.x>
- Lippincott-Schwartz, J., E. Snapp, and A. Kenworthy. 2001. Studying protein dynamics in living cells. *Nat. Rev. Mol. Cell Biol.* 2:444–456. <http://dx.doi.org/10.1038/35073068>
- Liu, P., Y. Ying, Y. Zhao, D.I. Mundy, M. Zhu, and R.G. Anderson. 2004. Chinese hamster ovary K2 cell lipid droplets appear to be metabolic organelles involved in membrane traffic. *J. Biol. Chem.* 279:3787–3792. <http://dx.doi.org/10.1074/jbc.M311945200>
- Marchesan, D., M. Rutberg, L. Andersson, L. Asp, T. Larsson, J. Borén, B.R. Johansson, and S.O. Olofsson. 2003. A phospholipase D-dependent process forms lipid droplets containing caveolin, adipocyte differentiation-related protein, and vimentin in a cell-free system. *J. Biol. Chem.* 278:27293–27300. <http://dx.doi.org/10.1074/jbc.M301430200>
- McMahon, H.T., and J.L. Gallop. 2005. Membrane curvature and mechanisms of dynamic cell membrane remodeling. *Nature*. 438:590–596. <http://dx.doi.org/10.1038/nature04396>

- Milewska, M., J. McRedmond, and P.C. Byrne. 2009. Identification of novel spartin-interactors shows spartin is a multifunctional protein. *J. Neurochem.* 111:1022–1030. <http://dx.doi.org/10.1111/j.1471-4159.2009.06382.x>
- Moessinger, C., L. Kuerschner, J. Spandl, A. Shevchenko, and C. Thiele. 2011. Human lysophosphatidylcholine acyltransferases 1 and 2 are located in lipid droplets where they catalyze the formation of phosphatidylcholine. *J. Biol. Chem.* 286:21330–21339. <http://dx.doi.org/10.1074/jbc.M110.202424>
- Nixon, S.J., R.I. Webb, M. Floetenmeyer, N. Schieber, H.P. Lo, and R.G. Parton. 2009. A single method for cryofixation and correlative light, electron microscopy and tomography of zebrafish embryos. *Traffic.* 10:131–136. <http://dx.doi.org/10.1111/j.1600-0854.2008.00859.x>
- Park, S.H., and C. Blackstone. 2010. Further assembly required: construction and dynamics of the endoplasmic reticulum network. *EMBO Rep.* 11:515–521. <http://dx.doi.org/10.1038/embor.2010.92>
- Ploegh, H.L. 2007. A lipid-based model for the creation of an escape hatch from the endoplasmic reticulum. *Nature.* 448:435–438. <http://dx.doi.org/10.1038/nature06004>
- Pol, A., S. Martin, M.A. Fernandez, C. Ferguson, A. Carozzi, R. Luetterforst, C. Enrich, and R.G. Parton. 2004. Dynamic and regulated association of caveolin with lipid bodies: modulation of lipid body motility and function by a dominant negative mutant. *Mol. Biol. Cell.* 15:99–110. <http://dx.doi.org/10.1091/mbc.E03-06-0368>
- Pol, A., S. Martin, M.A. Fernández, M. Ingelmo-Torres, C. Ferguson, C. Enrich, and R.G. Parton. 2005. Cholesterol and fatty acids regulate dynamic caveolin trafficking through the Golgi complex and between the cell surface and lipid bodies. *Mol. Biol. Cell.* 16:2091–2105. <http://dx.doi.org/10.1091/mbc.E04-08-0737>
- Poppelreuther, M., B. Rudolph, C. Du, R. Großmann, M. Becker, C. Thiele, R. Ehehalt, and J. Füllekrug. 2012. The N-terminal region of acyl-CoA synthetase 3 is essential for both the localization on lipid droplets and the function in fatty acid uptake. *J. Lipid Res.* 53:888–900. <http://dx.doi.org/10.1194/jlr.M024562>
- Richter, T., M. Floetenmeyer, C. Ferguson, J. Galea, J. Goh, M.R. Lindsay, G.P. Morgan, B.J. Marsh, and R.G. Parton. 2008. High-resolution 3D quantitative analysis of caveolar ultrastructure and caveola-cytoskeleton interactions. *Traffic.* 9:893–909. <http://dx.doi.org/10.1111/j.1600-0854.2008.00733.x>
- Robenek, H., O. Hofnagel, I. Buers, M.J. Robenek, D. Troyer, and N.J. Severs. 2006. Adipophilin-enriched domains in the ER membrane are sites of lipid droplet biogenesis. *J. Cell Sci.* 119:4215–4224. <http://dx.doi.org/10.1242/jcs.03191>
- Salo, V.T., Y. Ohsaki, and E. Ikonen. 2011. Lipid droplet biogenesis: when the endoplasmic reticulum starts to fatten up. *Curr. Opin. Lipidol.* 22:505–506. <http://dx.doi.org/10.1097/MOL.0b013e32834d1729>
- Sandoval, A., P. Fraisl, E. Arias-Barrau, C.C. Dirusso, D. Singer, W. Sealls, and P.N. Black. 2008. Fatty acid transport and activation and the expression patterns of genes involved in fatty acid trafficking. *Arch. Biochem. Biophys.* 477:363–371. <http://dx.doi.org/10.1016/j.abb.2008.06.010>
- Skinner, J.R., T.M. Shew, D.M. Schwartz, A. Tzekov, C.M. Lepus, N.A. Abumrad, and N.E. Wolins. 2009. Diacylglycerol enrichment of endoplasmic reticulum or lipid droplets recruits perilipin 3/TIP47 during lipid storage and mobilization. *J. Biol. Chem.* 284:30941–30948. <http://dx.doi.org/10.1074/jbc.M109.013995>
- Soni, K.G., G.A. Mardones, R. Sougrat, E. Smirnova, C.L. Jackson, and J.S. Bonifacino. 2009. Coatamer-dependent protein delivery to lipid droplets. *J. Cell Sci.* 122:1834–1841. <http://dx.doi.org/10.1242/jcs.045849>
- Soupe, E., and F.A. Kuypers. 2008. Mammalian long-chain acyl-CoA synthetases. *Exp. Biol. Med. (Maywood).* 233:507–521. <http://dx.doi.org/10.3181/0710-MR-287>
- Soupe, E., N.P. Dinh, M. Siliakus, and F.A. Kuypers. 2010. Activity of the acyl-CoA synthetase ACSL6 isoforms: role of the fatty acid Gate-domains. *BMC Biochem.* 11:18. <http://dx.doi.org/10.1186/1471-2091-11-18>
- Stone, S.J., M.C. Levin, P. Zhou, J. Han, T.C. Walther, and R.V. Farese Jr. 2009. The endoplasmic reticulum enzyme DGAT2 is found in mitochondria-associated membranes and has a mitochondrial targeting signal that promotes its association with mitochondria. *J. Biol. Chem.* 284:5352–5361. <http://dx.doi.org/10.1074/jbc.M805768200>
- Sturley, S.L., and M.M. Hussain. 2012. Lipid droplet formation on opposing sides of the endoplasmic reticulum. *J. Lipid Res.* 53:1800–1810. <http://dx.doi.org/10.1194/jlr.R028290>
- Suzuki, M., Y. Shinohara, Y. Ohsaki, and T. Fujimoto. 2011. Lipid droplets: size matters. *J. Electron Microsc. (Tokyo).* 60(Suppl 1):S101–S116. <http://dx.doi.org/10.1093/jmicro/df016>
- Turró, S., M. Ingelmo-Torres, J.M. Estanyol, F. Tebar, M.A. Fernández, C.V. Albor, K. Gaus, T. Grewal, C. Enrich, and A. Pol. 2006. Identification and characterization of associated with lipid droplet protein 1: A novel membrane-associated protein that resides on hepatic lipid droplets. *Traffic.* 7:1254–1269. <http://dx.doi.org/10.1111/j.1600-0854.2006.00465.x>
- Walther, T.C., and R.V. Farese Jr. 2009. The life of lipid droplets. *Biochim. Biophys. Acta.* 1791:459–466. <http://dx.doi.org/10.1016/j.bbali.2008.10.009>
- Walther, T.C., and R.V. Farese Jr. 2012. Lipid droplets and cellular lipid metabolism. *Annu. Rev. Biochem.* 81:687–714. <http://dx.doi.org/10.1146/annurev-biochem-061009-102430>
- Wang, C.W., and S.C. Lee. 2012. The ubiquitin-like (UBX)-domain-containing protein Ubx2/Ubx8 regulates lipid droplet homeostasis. *J. Cell Sci.* 125:2930–2939. <http://dx.doi.org/10.1242/jcs.100230>
- Wanner, G., H. Formanek, and R.R. Theimer. 1981. The ontogeny of lipid bodies (sphaerosomes) in plant cells: Ultrastructural evidence. *Planta.* 151:109–123. <http://dx.doi.org/10.1007/BF00387812>
- Welte, M.A. 2007. Proteins under new management: lipid droplets deliver. *Trends Cell Biol.* 17:363–369. <http://dx.doi.org/10.1016/j.tcb.2007.06.004>
- Wilfling, F., H. Wang, J.T. Haas, N. Kraemer, T.J. Gould, A. Uchida, J.X. Cheng, M. Graham, R. Christiano, F. Fröhlich, et al. 2013. Triacylglycerol synthesis enzymes mediate lipid droplet growth by relocalizing from the ER to lipid droplets. *Dev. Cell.* 24:384–399. <http://dx.doi.org/10.1016/j.devcel.2013.01.013>
- Wolins, N.E., B.K. Quaynor, J.R. Skinner, M.J. Schoenfish, A. Tzekov, and P.E. Bickel. 2005. S3-12, Adipophilin, and TIP47 package lipid in adipocytes. *J. Biol. Chem.* 280:19146–19155. <http://dx.doi.org/10.1074/jbc.M500978200>
- Zanghellini, J., F. Wodlei, and H.H. von Grünberg. 2010. Phospholipid demixing and the birth of a lipid droplet. *J. Theor. Biol.* 264:952–961. <http://dx.doi.org/10.1016/j.jtbi.2010.02.025>
- Zehmer, J.K., R. Bartz, P. Liu, and R.G. Anderson. 2008. Identification of a novel N-terminal hydrophobic sequence that targets proteins to lipid droplets. *J. Cell Sci.* 121:1852–1860. <http://dx.doi.org/10.1242/jcs.012013>

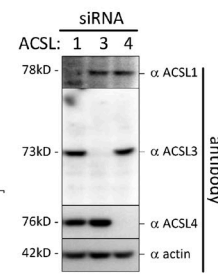
Levels of ACSL family members in different cell types



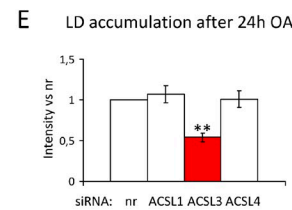
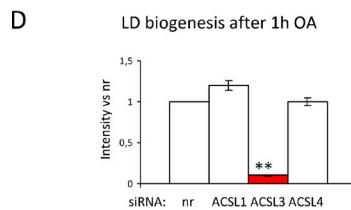
Levels of ACSL family members after siRNA



ACSL proteins levels after siRNA



Role of ACSL family members in LD biogenesis and accumulation after down-regulation (flow cytometry)



Role of ACSL family members in LD biogenesis and accumulation after overexpression (flow cytometry)

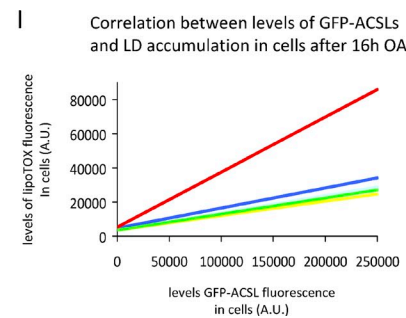
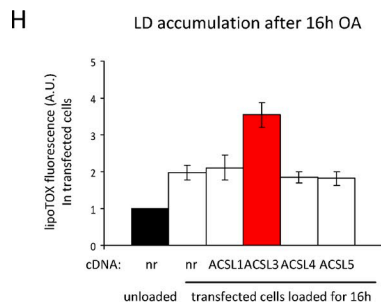
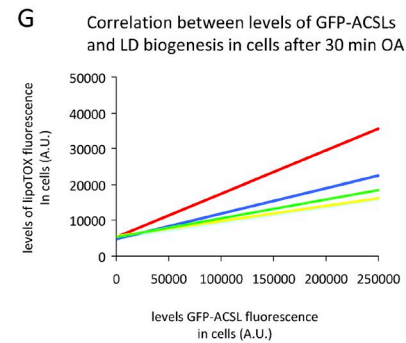
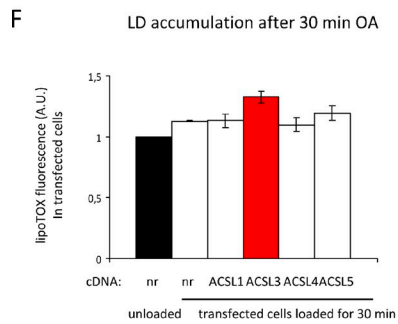


Figure S2. Role of other ACSL family members in LD assembly and neutral lipid accumulation. This figure is a supplement to Fig. 7. (A) The relative expression levels of ACSL3 in the cell lines used in this study (see hepatic cells in Fig. S4) was compared with the expression of other ACSL family members by qRT-PCR (the value of ACSL3 in each cell line was normalized to 1). (B and C) COS-1 cells were transfected for 24 h with the siRNA corresponding to ACSL1, ACSL3, or ACSL4 and then additionally starved for 24 h. The percentage of RNA expression levels of each isoform at this time point, with respect to a nonrelated siRNA (nr), was determined by real-time PCR (B), and the specificity of each siRNA for the corresponding family member confirmed by Western blotting of cell homogenates (C). (D and E) Next, neutral lipids were quantified with Nile red and flow cytometry in the siRNA-transfected cells after the starvation period and after an additional treatment with OA for 1 h (D) or 24 h (E). **, $P < 0.01$. (F–I) To demonstrate that only ACSL3 determines LD levels, even when the ACSL enzymes are expressed to identical levels, COS-1 cells were transfected with the indicated GFP-tagged ACSL isoforms or with the GFP and starved for 24 h. Cells were then treated with OA for 30 min (F and G) or 16 h (H and I). LDs were labeled using LipidTOX Deep red, and the transfected cells were identified in the flow cytometer by the presence of green fluorescence. The graphs in F and H show the mean intensity of LDs (red fluorescence) in transfected cells (GFP positive), quantified in three independent experiments and normalized to the red fluorescence of unloaded GFP-transfected cells. The graphs in G and I show a representative trend line of the red fluorescence (LD levels) quantified in cells with increasing levels of expression of each GFP-ACSL (green fluorescence intensity). Altogether, these results demonstrate that ACSL3 is the family member that determines biogenesis and accumulation of LDs in COS-1 cells. Error bars indicate the standard deviation of at least three independent experiments.

Generation of a siRNA-resistant and an inactive forms of ACSL3

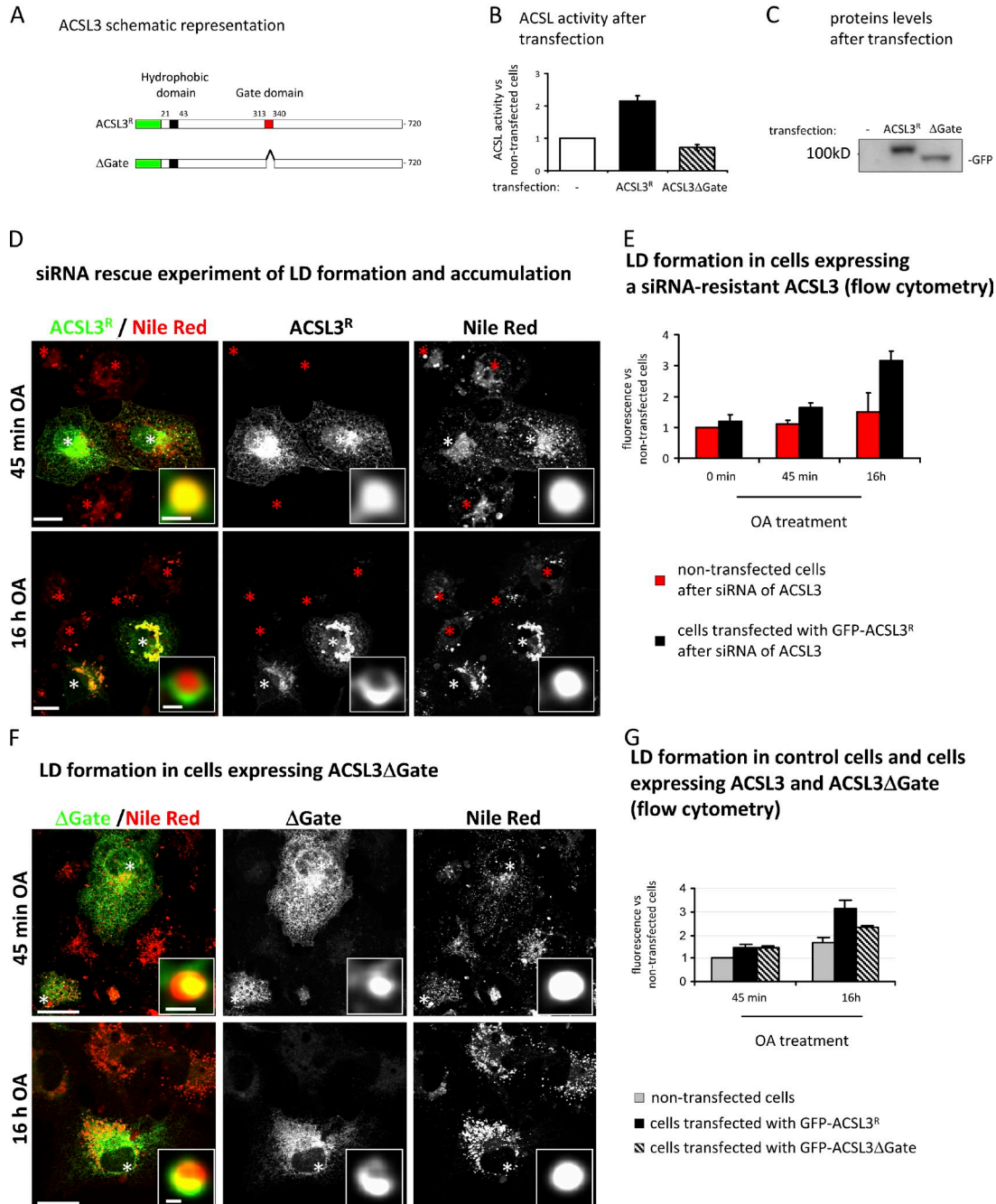
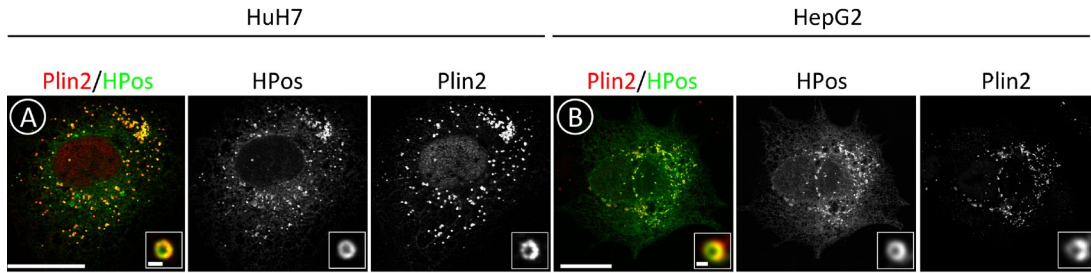
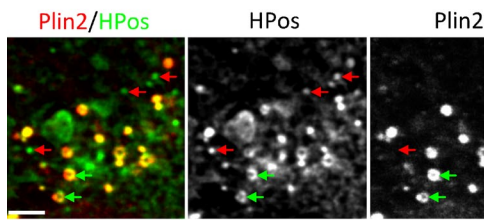


Figure S3. **siRNA rescue experiment and the likely scaffolding role of ACSL3 during LD biogenesis.** This figure is a supplement to Fig. 7. (A) Schematic representation of the proteins used in the figure; an siRNA-resistant form of ACSL3 (ACSL3^R) and an inactive form of ACSL3 generated by deletion of the residues corresponding to the Gate domain (ACSL3ΔGate). Although no conclusive structural information is available for the mammalian acyl-CoA synthetases (Soupene and Kuypers, 2008), in the specific case of ACSL6, the fatty acid Gate domain motif is essential for the activity of the human isoform (Soupene et al., 2010). Because this region is conserved in mammalian ACSLs, we generated a GFP-tagged ACSL3 without the Gate domain (red letters in Fig. S5 B). (B and C) The acyl-CoA synthetase activity was quantified in control COS-1 cells and in cells additionally transfected with ACSL3^R or ACSL3ΔGate. In contrast to the full-length GFP-ACSL3, the GFP-ACSL3ΔGate did not demonstrate detectable enzymatic activity (B), although the expression of both proteins was similar when analyzed by Western blotting of cell homogenates with anti-GFP antibodies (C). (D and E) To rule out off-target effects of the siRNAs used in this study, starved ACSL3-depleted cells, by means of the siRNA, were transfected for 24 h with ACSL3^R and then incubated for 45 min or 16 h with OA. Neutral lipids were labeled with Nile red and analyzed by confocal microscopy (D) or with LipidTOX and flow cytometry (E). The expression of ACSL3^R rescued the inhibition caused by the siRNA of ACSL3 in the assembly and accumulation of LDs. The insets show representative emerging and mature LDs, and the asterisks indicate the transfected cells. (F and G) Finally, starved ACSL3ΔGate-transfected cells were also incubated for 45 min or 16 h with OA, and neutral lipids were stained with Nile red and analyzed by microscopy (F) or with LipidTOX and flow cytometry (G). After 45 min, the ACSL3ΔGate-transfected cells demonstrated an increased accumulation of LDs when compared with cells transfected with GFP, which was similar to the increment caused by the full-length GFP-tagged ACSL3. The ACSL3ΔGate-expressing cells also demonstrated a relative increase in neutral lipid accumulation when treated with OA for 16 h. This lends support to the hypothesis that not only the enzymatic activity of ACSL3 but also other properties of the enzyme cooperate during LD nucleation, and that the activity of the enzyme is involved in LD growth and expansion (see Discussion). The GFP-ACSL3ΔGate showed a preferential accumulation in one side of the LDs (high-magnification insets in F), which suggests that the fatty acid Gate domain partially determines the transport of the enzyme into LDs. White asterisks indicate transfected cells. Bars: (main panels) 25 μm; (insets) 2 μm. Error bars indicate the standard deviation of at least three independent experiments.

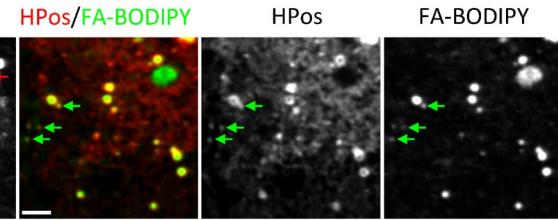
LDs in hepatic cells 48 hours after starvation



C Plin2 and HPos in LDs of hepatic cells

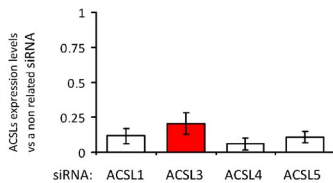


D Lipid incorporation into LDs of hepatic cells

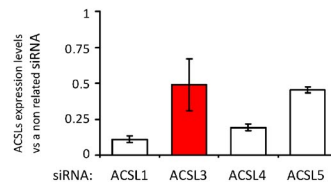


Down-regulation of ACSL family members in hepatic cell lines by siRNA

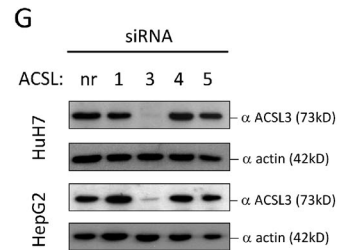
E Expression of ACSLs after specific siRNA in HuH7 cells (rtPCR)



F Expression of ACSLs after specific siRNA in HepG2 cells (rtPCR)

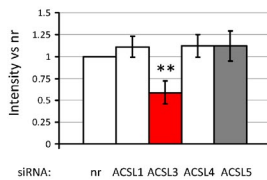


ACSL3 expression levels after siRNA

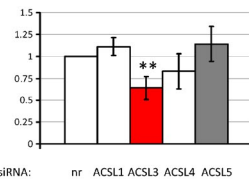


Role of ACSL family members in LD biogenesis and accumulation in hepatic cell lines (flow cytometry)

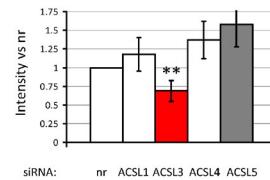
H LD biogenesis in HuH7 1h OA



I LD accumulation in HuH7 24h OA



J LD biogenesis in HepG2 1h OA



K LD accumulation in HepG2 24h OA

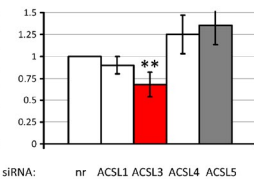
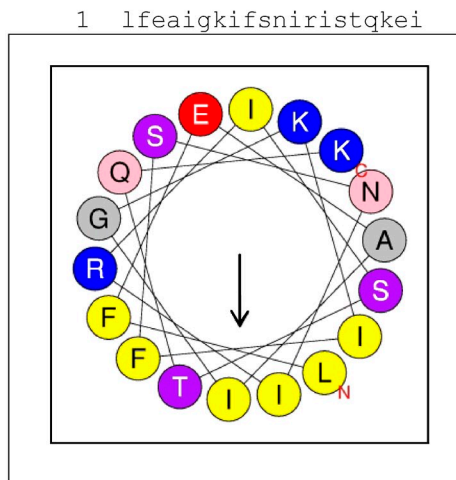


Figure S4. **ACSL3 regulates LD assembly and neutral lipid accumulation in hepatic cell lines.** This figure is a supplement to Fig. 7. To analyze the role of ACSL3 during LD formation and accumulation in other cell lines, we tested the effect of the ACSLs siRNA in human hepatic cell lines, such as HuH7 and HepG2. (A–C) First, GFP-HPos–transfected HuH7 (A and C) and HepG2 (B) cells were starved for 48 h. Distributions of HPos (green) and endogenous Plin2 (red) were analyzed by confocal microscopy. The images show that the starvation conditions that efficiently removed LDs in COS-1 cells did not completely eliminate the presence of LDs in hepatic cells even when prolonged for 48 h. In contrast to the pre-LDs of COS-1 cells, the number of LDs observed in hepatic cells after starvation was partially reduced by Triacsin C or Platensimycin, a specific inhibitor of the fatty acid synthase (not depicted), which suggests that during starvation these LDs are supplied with newly synthesized fatty acids. After 48 h of starvation, HPos formed a characteristic ring around mature LDs that colocalized with endogenous Plin2 (A, B, and green arrows in C). The red arrows indicate HPos-positive but Plin2-negative structures. Thus, several structures positive for HPos and negative for Plin2, which could be equivalent to the pre-LDs observed in COS-1 cells, are also present in hepatic cells (C, red arrows). The insets show a representative mature LD. Bars: (A and B) 25 μ m; (insets) 0.5 μ m; (C) 2 μ m. (D) To analyze lipid packaging in these cells, OFP-HPos–transfected HuH7 cells were treated as in Fig. 4 with the FA-BODIPY for 15 min. Cells were fixed, and lipid distribution was analyzed by microscopy. The green arrows indicate that the FA-BODIPY was rapidly packed in the small HPos-positive LDs and in the mature LDs. Bar, 2 μ m. (E–K) To study the role of ACSL3 during lipid packaging, HuH7 and HepG2 cells were transfected for 24 h with the siRNAs corresponding to ACSL1, ACSL3, ACSL4, or ACSL5 and then additionally starved for 24 h. The RNA levels after each siRNA were measured by real-time PCR (A and B) and shown in the graph as a percentage with respect to cells transfected with a nonrelated siRNA (nr). The ACSL3 protein levels were additionally analyzed by Western blotting of cell homogenates (G). The cells were then loaded for 1 h or 24 h with OA, neutral lipids were stained with Nile red, and cellular fluorescence was quantified by flow cytometry. Only when ACSL3, but not other family members, was down-regulated were the early accumulation of neutral lipids and the long-term accumulation of LDs significantly reduced, which suggests that ACSL3 is the family member that regulates LD formation and accumulation in hepatic cell lines. Error bars indicate the standard deviation of at least three independent experiments. **, $P < 0.01$.

A
Amino acid sequence and *in silico* analysis of alpha-helix formation by the positive sequence of HPos



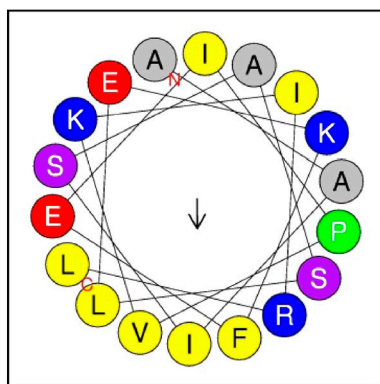
B
Amino acid sequence and examples of *in silico* analysis of alpha-helix formation by human ACSL3

```

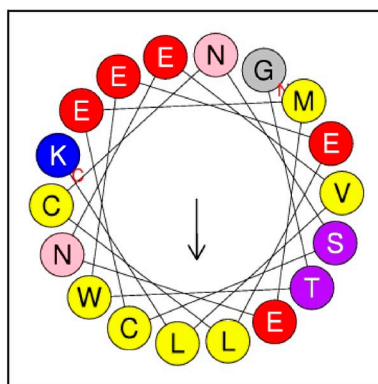
1 mnhvsskps tmklkhtinp illyfihfli slytiltyip fyffsesrqe ksnrikakpv
61 nskpdsayrs vnsldglasv lypgcdtldk vftyaknkfk nkrlldgtrev lneedeveqpn
121 gkifkkvilg qynwlsyedv fvrafnfgng lqmlgqkpkt niaifcetra ewmiaaqacf
181 mynflvtly atlggpaivh alnetevtni itskellqtk lkdivslvpr lrhiitvdgk
241 pptwsefpkg iivhtmaave algakasmn qphskplpsd iavimytsgs tglpkgvms
301 hsniiagitg maeripelge edvyigypl ahvlelsael vclshgcrig ysspqtldq
361 sskikksgk dtsmlkptlm aavpeimdri yknvmkvse mssfqrnlfi laynykmeqi
421 skgrntplcd sfvfrkvrsl lggnrlllc ggapslattq rfmnicfccp vgggygltes
481 agagtisev dyntgrvgap lvcceiklkn weeggyfntd kphprgeili ggqsvtmgyy
541 kneaktkadf fedengqrwl ctgdigefep dgclkiidrk kdvlklqage yvslgkveaa
601 lknplvdni cayansyhsy vigfvvpnqk eltelarkkg lkgtweelcn scemenevlk
661 vlseaaisas lekfeipvki rlspepwtpe tglvtdafkl krkelkthyq adiermygrk

```

AAISASLEKFEIPVKIRL¹⁴²



GTWEELCNSCEMENEVLK¹²⁰



VIGFVVPNQKELTELARK⁹⁸

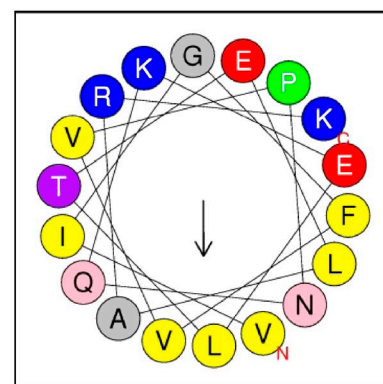
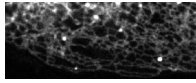
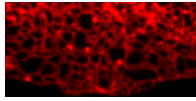


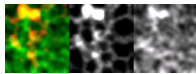
Figure S5. **Putative amphipathic α helices in HPos and ACSL3.** This figure is a supplement to the Discussion section. The figure shows the amino acid sequence and the *in silico* analysis of putative amphipathic α helices predicted by the HELIQUEST program (<http://heliquest.ipmc.cnrs.fr/>) to be formed by HPos and the human form of ACSL3 (three representative sequences; Gautier et al., 2008). In each helix, the hydrophobic amino acids (yellow) are enriched on the opposite side to negative (red) and positive (blue) residues.



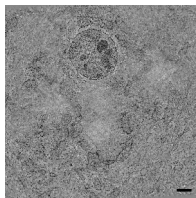
Video 1. **Starved GFP-HPos-transfected COS-1 cells were treated with cycloheximide for 30 min.** This video corresponds to Fig. 3 A. Images were analyzed by time-lapse confocal microscopy using a laser scanning confocal spectral microscope (TCS SP5; Leica) equipped with an incubation control system (37°C, 5% CO₂). Cells were selected for the labeling of well-defined tubular ER elements. In starved cells, pre-LDs were followed for 5 min (images were captured every 1.3 s). Next, OA (175 µg/ml) was added (indicated with OA in left bottom corner) and images were captured for an additional 15 min every 9 s.



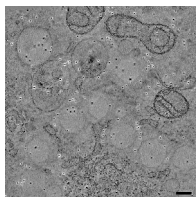
Video 2. **Images of starved COS-1 cells transfected with orange-HPos (red) were analyzed by time-lapse confocal microscopy using a laser scanning confocal spectral microscope (TCS SP5; Leica) equipped with an incubation control system (37°C, 5% CO₂).** This video corresponds to Fig. 2 A (merged channels). Cells were selected for the labeling of well-defined tubular ER elements. In starved cells, pre-LDs were followed for 5 min (images were captured every 1.3 s). Cells were then loaded with OA (175 µg/ml) that additionally contained a BODIPY-tagged fatty acid (1 µM, green). Images were captured for an additional 15 min every 9 s.



Video 3. **The three channels (merge channels, red for HPos, and green for FA-BODIPY) of two selected pre-LDs and one emerging LD shown in Video 2.** This video corresponds to Fig. 2 A (separated channels). As in Video 2, starved COS-1 cells transfected with orange-HPos (red) were analyzed using a laser-scanning confocal spectral microscope (TCS SP5; Leica). Cells were selected for the labeling of well-defined tubular ER elements. In starved cells, pre-LDs were followed for 5 min (images were captured every 1.3 s). Cells were then loaded with OA (175 µg/ml) that additionally contained a BODIPY-tagged fatty acid (1 µM, green). Images were captured for an additional 15 min every 9 s.



Video 4. **Starved COS-1 cells were treated for 10 min with OA and then submitted to a second starvation for an additional 16 h.** This video corresponds to Fig. 9. Cells were processed with no primary fixative and a very quick nonperturbing freeze substitution protocol. 300-nm HM20 sections, nonspecifically labeled with gold as fiducial markers, were tilted $\pm 60^\circ$ in both axes, taking images every 1 or 2° using an intermediate-voltage EM (Tecnai F30; FEI Company). Bars, 250 nm.



Video 5. **Starved COS-1 cells were treated for 10 min with OA and then submitted to a second starvation for an additional 16 h.** This video corresponds to Fig. 9. Cells were processed with no primary fixative and a very quick nonperturbing freeze substitution protocol. 300-nm HM20 sections, nonspecifically labeled with gold as fiducial markers, were tilted $\pm 60^\circ$ in both axes taking images every 1 or 2° using an intermediate voltage EM (Tecnai F30; FEI Company). Bars, 250 nm.

References

- Gautier, R., D. Douguet, B. Antonny, and G. Drin. 2008. HELIQUEST: a web server to screen sequences with specific alpha-helical properties. *Bioinformatics*. 24:2101–2102. <http://dx.doi.org/10.1093/bioinformatics/btn392>
- Soupene, E., and F.A. Kuypers. 2008. Mammalian long-chain acyl-CoA synthetases. *Exp. Biol. Med. (Maywood)*. 233:507–521. <http://dx.doi.org/10.3181/0710-MR-287>
- Soupene, E., N.P. Dinh, M. Siliakus, and F.A. Kuypers. 2010. Activity of the acyl-CoA synthetase ACSL6 isoforms: role of the fatty acid Gate-domains. *BMC Biochem*. 11:18. <http://dx.doi.org/10.1186/1471-2091-11-18>